

SO₂ gas reactions with silicate glasses

Christian J. Renggli and Penelope L. King

Research School of Earth Sciences

The Australian National University

Canberra, ACT 2601, Australia

christian.renggli@anu.edu.au, penny.king@anu.edu.au

INTRODUCTION

Sulfur dioxide (SO_{2(g)}) is an important gas species in most common volcanic settings on Earth including subduction zones (Shinohara 2013). The relative abundances of SO_{2(g)} may vary at a volcano over time with the highest rates of SO_{2(g)} emissions occurring during eruptive degassing and lesser amounts emitted continuously during quiescent degassing, resulting in a large total amount of SO_{2(g)} integrated over time of the order of 10 Mt/a (McCormick et al. 2013; Shinohara 2013; Henley and Hughes 2016). Much of the emitted SO_{2(g)} is released at high temperatures. For instance, gas mixtures sampled at the highest temperature volcanic vents reach 1131 °C at Erta Ale volcano and these are the most likely to be representative of the volcanic gas phase (de Moor et al. 2013).

SO_{2(g)} is the most abundant of the corrosive gases at volcanoes (Oppenheimer et al. 2014). In the 1970's, thermodynamic models were used to predict that SO_{2(g)} reactions with silicates form sulfate and reduced sulfur (Gooding 1978; Burnham 1979). This was later shown experimentally through reactions of silicates and carbonates with SO_{2(g)} (Fegley and Prinn 1989; Burnett et al. 1997). When SO_{2(g)} reacts with silicates it covalently binds to the solid surface to build up a surface coating (Henley et al. 2015). In this manner, the SO_{2(g)} reaction fundamentally differs from ionic reactions with some of the other species common in volcanic settings such as H₂O-rich fluids (e.g. Oelkers and Schott 2009) or carbon dioxide (DePaolo and Cole 2013). Other species common in volcanic gases such as fluorine and chlorine are also important (Delmelle et al. 2018, this volume, Henley and Seward 2018, this volume), but sulfur gases have particularly interesting properties because sulfur is a multivalent element. Several valence states are involved in SO_{2(g)} reactions with aluminosilicate glasses (S⁻², S⁻¹, S⁰, S⁴⁺ and S⁶⁺). These different species add complexity to the reactions because they may affect the valence state of other multivalent cations in the solid (e.g., Fe^{0/2+/3+}, Ti^{3+/4+}, Cr^{2+/3+}, V^{2+/3+/4+/5+}, Eu^{2+/3+}).

Gaseous sulfur dioxide has been detected on a number of other planetary bodies. For example, on Jupiter's moon, Io, SO_{2(g)} is emitted by large explosive eruptions and contributes to a transient S-rich atmosphere (Kumar 1985; Johnson and Burnett 1993; Burnett et al. 1997; Doute 2002). SO_{2(g)} occurs as a minor volcanogenic gas species in the atmosphere of Venus, where it may play an important role in the alteration of the planet's surface (Zolotov 2018, this volume). On Mars, the regolith and dust are rich in oxidized sulfur (e.g., Berger et al. 2016) suggesting that past volcanic eruptions were rich in SO_{2(g)} (King and McLennan 2010; Franz et al. 2017). Because SO_{2(g)} dominantly forms in volcanic eruptions, it may be a good proxy for past or ongoing volcanic activity in planetary and exoplanet atmospheres (Hu et al. 2013; Misra et al. 2015). Reactions between gases, including SO_{2(g)}, and solids occurring in the solar system are discussed by Sossi et al. (2018, this volume) and Zolotov (2018, this volume).

In this chapter we discuss observations from gas-solid experiments where SO_{2(g)} is reacted with aluminosilicate glasses. The understanding of SO_{2(g)} reactions with glasses is important because of their ubiquity in volcanic systems (Ayrís et al. 2013; Delmelle et al. 2018) and their

1 abundance on planetary surfaces due to impact processes (Schultz and Mustard, 2004). We discuss
2 the chemistry, mineralogy and texture of the reaction products, as well as provide insights into
3 reaction mechanisms.

4 **GLASS PROPERTIES**

5 Silicate glasses are an ideal substrate material to study gas-silicate reactions because they
6 are amorphous, which avoids complications from mineral orientation effects. To provide context
7 for $\text{SO}_{2(g)}$ reactions with glass, we refer the reader to King et al. (2018) for a review of the basic
8 reactions between $\text{SO}_{2(g)}$ and silicate minerals.

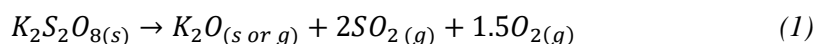
9 Aluminosilicate glasses are dominated by Si^{4+} and Al^{3+} cations that are tetrahedrally-
10 coordinated by O^{2-} anions and termed tetrahedral cations (T) (Mysen and Richet 2005). The T
11 cations (in some cases including Ti^{4+} and Fe^{3+}) form a range of Si-O units (e.g., $[\text{SiO}_4]^{4-}$, $[\text{Si}_2\text{O}_7]^{6-}$,
12 $[\text{Si}_6\text{O}_{18}]^{12-}$, $[\text{Si}_4\text{O}_{11}]^{6-}$, $[\text{Si}_2\text{O}_5]^{2-}$, $[\text{SiO}_2]$). These units are polymerized to form a network linked by
13 a distribution of bond lengths and bond angles with a lack of long-range order. Monovalent and
14 divalent cations (e.g., Na^+ , K^+ , Mg^{2+} and Ca^{2+}) have a role as network modifiers and/or charge
15 compensators and do not contribute to the tetrahedral network (Mysen et al. 1982; Mysen and
16 Richet 2005).

17 The structural arrangement of atoms in a silicate glass is of great importance for the
18 physical properties, including structure and degree of polymerization, viscosity, glass transition
19 temperature and diffusion rates (Dingwell 2006). The main variable affecting glass properties is
20 the concentration of network-forming cations, the most abundant of which are Si^{4+} and Al^{3+} .
21 Network-forming cations exhibit a low mobility and their self-diffusivities are a function of the
22 melt's viscosity, and can be described by the Eyring equation (Dingwell 1990). Relative to network
23 formers, network modifiers have diffusivities that are orders of magnitude higher (Dingwell 1990).
24 More recently, the identification of charge compensating cations (e.g. Na, K, Ca) in simple glasses
25 has shown that these elements may move in channels, which allows a more complex element
26 mobility (Le Losq et al. 2017).

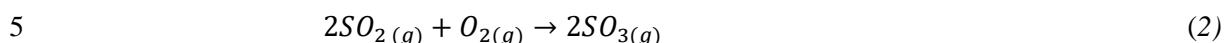
27 Temperature plays an important role in element mobility (Zhang 2010) and in glasses, the
28 glass transition temperature is a key reference point. The glass transition is the temperature range
29 below which the amorphous structure is locked in and becomes unrelaxed and the material behaves
30 as a solid. As a consequence, configurational changes do not occur on a measurable scale below
31 the glass transition temperature and the energetically most favorable state is not reached (Mysen
32 and Richet 2005). The glass transition is a function of the relaxation of the network of Si-O units
33 and hence of the lifetime of the bonds (e.g., Webb 1997). The temperature range from 600 to
34 850 °C, at which $\text{SO}_{2(g)}$ reactions with silicate glasses have been performed experimentally (Tables
35 1 and 2), is near the glass transitions of these systems (Martens et al. 1987; Knoche et al. 1992).
36 Consequently, minor changes in the temperature conditions may affect the reaction rates and
37 mechanisms considerably when the glass transition is crossed.

38 **EXPERIMENTAL TECHNIQUES**

39 Experiments reacting $\text{SO}_{2(g)}$ with silicate glasses have been performed with both open and
40 closed systems. Early experiments were performed in closed systems, in respect to the glass, in
41 sealed silica tubes where $\text{SO}_{2(g)}$ was produced via the decomposition of $\text{K}_2\text{S}_2\text{O}_8$. The decomposition
42 of this compound forms $\text{SO}_{2(g)}$ and $\text{O}_{2(g)}$ (Johnson and Burnett 1993; Li et al. 2010) via Equation
43 (1):

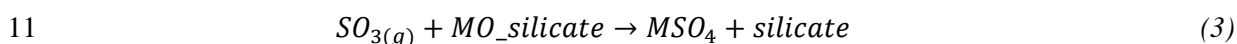


1 In reaction 1, K₂O occurs as either a solid or gas species dependent on temperature and pressure
2 (e.g., Muam and Osborn, 1965). As the sample is cooled, solid K₂O may be deposited in the tube
3 and on the silicate sample. Removal of K₂O as a solid from the experimental system, will tend to
4 favor the reaction:

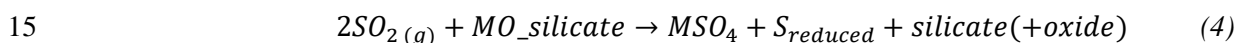


6 This reaction lowers the fugacity of SO_{2(g)}, creating an environment where SO_{3(g)} is an important
7 reactant and the reaction products are changed. Thus, to examine pure SO_{2(g)}, it is necessary to trap
8 or remove the O_{2(g)} if the gases are produced via Equation (1) (Burnett et al. 1997).

9 Monitoring of the SO_{2(g)}/SO_{3(g)} in the gas phase is important because SO_{3(g)}-mineral
10 reactions follow the general form:



12 where M is a cation (e.g., Ca, Mg, Na, and Fe) and S remains in the 6+ state. In contrast, in SO_{2(g)}-
13 mineral reactions, where S⁴⁺ in the gas phase disproportionates into 6+ and reduced sulfur (e.g., S²⁻
14 , a reduced sulfur radical, S⁻ or S⁰), the reaction follows the form (modified after Burnham 1979):



16 To avoid the issues associated with K₂S₂O₈ decomposition, recent experiments used
17 commercial SO_{2(g)} as the gas source (Tables 1 & 2; King et al. 2018, this volume). A Gibbs Free
18 Energy minimization calculation reveals that SO_{2(g)} is not pure at equilibrium conditions, even
19 under the assumption that the gas source is pure. We used the software package HSC8 by Outotec,
20 which is based on the JANAF database (Chase 1998). The most abundant trace gas species in
21 equilibrium with SO_{2(g)} are SO_{3(g)}, SO_(g) and S_{2(g)} (Fig. 1). All trace species have abundances of less
22 than 10⁻⁵ mole fractions in the temperature range relevant to studies involving the reaction of SO_{2(g)}
23 (600-850 °C, see tables 1 and 2). The oxygen fugacity of this gas mixture is approximately at the
24 magnetite-hematite buffer in the temperature range relevant to the experiments discussed here. It
25 has been noted that the equilibration of the gas species in this system (SO_{2(g)}, SO_{3(g)}, O_{2(g)}) is
26 relatively slow (Luthra and Worrell 1979). Therefore, actual abundances of trace gases may be
27 even lower in these experiments because at the high flow rates of 20-50 cm³ per minute, equilibrium
28 speciation in the gas phase may not be attained. Changes in the composition of the gas during the
29 reaction have not been determined in any experiment.

30 Solid glass for experiments is best polished prior to reactions with SO_{2(g)} so that the run
31 products are easier to examine and to minimize artefacts. For example, gas-solid reactions are
32 sensitive to the surface area, and so cracks and scratches may result in a higher degree of reaction.
33 Furthermore, irregularities on the surface may act as nucleation points for sulfate formation on the
34 surface (Fig. 2, Burnett et al. 1997). Additional details on experimental setups are given in Chapter
35 1 (King et al. 2018, this volume).

36 **SO_{2(g)} REACTIONS WITH FE-FREE SILICATE GLASSES**

37 As indicated above, sulfur has many different valence states. This means that there can be
38 considerable complexity in reactions between SO_{2(g)} and multivalent cations, such as Fe, the most
39 abundant multivalent element in most magmatic systems (Schreiber 1987). We therefore separate
40 our discussion of experiments into either Fe-free or Fe-bearing glasses.

41 **Mineralogy of phases formed on Fe-free glass substrates**

42 Table 1 summarizes experiments on SO_{2(g)} reacted with synthetic Fe-free glasses from both
43 the literature and our laboratory. Compositions include glasses in the albite-anorthite-diopside
44 (Ab-An-Di) system, Fe-free basalt, soda-lime (Na-Ca-silicate) glass, and albite-orthoclase glass.

1 Temperature conditions range from 600-850 °C and experimental durations vary considerably
2 from 1 to 1366 hours. The run products include Na-, Ca- and/or Mg-sulfates.

3 The observation and determination of the mineralogy of products formed in SO_{2(g)}
4 experiments is challenging due to small grain sizes (Dalby et al. 2018; Palm et al. 2018). Reaction
5 products may have grain diameters of tens of nanometers, which are far below the resolution of
6 conventional methods such as Raman spectroscopy or energy dispersive X-ray spectroscopy. When
7 the reaction products are thinner than the analytical volume of the method used, the signal includes
8 both the reaction product and the silicate substrate. Such reaction products require high resolution
9 techniques such as transmission electron microscopy, atom probe microscopy, surface sensitive
10 analysis (e.g., X-ray photoelectron spectroscopy) or thin film approaches such as grazing angle
11 techniques or depth profiling (Dalby et al. 2018; Palm et al. 2018).

12 As the majority of reaction products from SO_{2(g)}-silicate reactions are sulfates, a brief
13 overview of sulfate phase relations is necessary (see also King et al. 2018, this volume). At elevated
14 temperatures, sulfates ultimately decompose into oxides and SO_{3(g)} (Stern 2001). For example,
15 MgSO₄ decomposes at temperatures above 900 °C and CaSO₄ above 1200 °C (Rowe et al. 1967;
16 Du 2000). In addition to thermal decomposition some sulfates may also vaporize at high
17 temperatures (e.g. $Na_2SO_{4(s)} = Na_2SO_{4(g)}$) (Stern and Weise 1966). At 600-800 °C, at which
18 most SO_{2(g)}-reaction experiments have been performed (see table 1 and 2), some of the sulfates
19 form limited solid solutions. The degree of solid solubility of Na₂SO₄ in CaSO₄ is poorly
20 understood as experimental data is limited. In turn, Na₂SO₄ dissolves up to 35 mol.% of CaSO₄ and
21 Na₂Ca(SO₄)₂ (glauberite) also forms (Freyer and Voigt 2003). Similarly, it also dissolves MgSO₄
22 although in a more limited temperature range. Na₂SO₄ and K₂SO₄ form a complete solid solution
23 from 600 to 800 °C. CaSO₄ and MgSO₄ do not form solid solutions. Instead, the binary system
24 includes the phase CaMg₃(SO₄)₄ (Rowe et al. 1967; Du 2000); this phase has not been reported in
25 any SO_{2(g)} experiment (Table 1). In these experimental studies the reporting of sulfates has
26 generally identified only the pure end-member phases.

27 The interpretation of sulfate textures formed in SO_{2(g)} reactions can be challenging due to
28 the hydrophilic nature of the materials. Magnesium sulfate in particular readily hydrates, forming
29 a large range of phases with various degrees of hydration (Wang et al. 2006). It is therefore crucial
30 to protect experimental samples from water vapor after the reaction (e.g., in a desiccator or under
31 controlled atmosphere). Even so, sulfates textures may evolve with time during sample storage and
32 hydrate in air (Dalby et al. 2018, this volume).

33 Textures of sulfate coatings on Fe-free glass substrates

34 The textures of sulfates observed on Fe-free glasses vary strongly with the glass
35 composition and experimental conditions. The sulfates form on the surfaces and are coating the
36 glasses. In the oxidation community these types of reaction products are termed scales (Birks et al.
37 2006), but we use the term coating, which is consistent with the use in the geological literature.
38 Sulfate surface coatings fall into two distinct categories of continuous and discontinuous coverage.
39 Electron microscopy images of these textures are shown in Figures 2, 3, 4 and 5. Discontinuously
40 distributed sulfates commonly display distinct crystal facets (Fig. 2 and 3). A secondary electron
41 images of a sulfate texture with discontinuous coverage is shown from an experiment with albite
42 glass (Fig. 3a, 600 °C, 1hour). This type of discontinuous coating occurs on albite glasses reacted
43 with SO_{2(g)} at 600-800 °C and experimental durations of 1 hour and 24 hours (table 1). Similarly
44 well-defined sulfate crystals have been observed on soda-lime and obsidian glasses (Burnett et al.
45 1997). The mechanism of sulfate growth in the case of discontinuous coatings is relatively simple,
46 because the glass surface remains exposed to the gas throughout the reaction as illustrated in Figure
47 3.

48 In experiments where the temperatures approach the thermal stability of the sulfates, the
49 individual sulfate “islands” are poorly crystallized and can be polycrystalline and flakey in texture

1 (Johnson and Burnett 1993). Formed in sealed silica glass tubes, such sulfates may be the product
2 of deposition from the gas phase or the quench product of a sulfate melt (Johnson and Burnett
3 1993). In experiments where these textures formed in a gas-furnace under a high $\text{SO}_{2(g)}$ flux, and
4 at temperatures below the liquidus temperature of the sulfate, the formation as quench products is
5 not possible and the textures are likely due to very high sulfate nucleation rates which exceed the
6 rates of grain growth.

7 Continuously-distributed sulfate coatings occur on a range of Fe-free experiments,
8 including Fe-free basalt and glasses in the Ab-An-Di ternary system. Anhydrite is commonly
9 distributed in a single layer of equigranular columnar grains, such as on anorthite glass (Fig. 4a,
10 800 °C, 1h). For Fe-free basalts, the surface material consists of a mixture of CaSO_4 and MgSO_4 .
11 The back-scattered electron image (Fig. 4b) of Fe-free basalt glass (700 °C, 24h) shows areas of
12 darker MgSO_4 , partially hydrated after the experiment, and rhombohedral anhydrite grains. The
13 textures of the continuous coatings have many similarities with coatings formed during the
14 oxidation in a range of systems, such as aluminum oxide scales on metal alloys (Hsueh and Evans
15 1983; Evans et al. 1983; Tolpygo and Clarke 1998a, b; Chason et al. 2013). A comparison of the
16 sulfate coatings with extensively studied oxide coatings is valuable as it allows an interpretation of
17 the mechanism that form these coatings.

18 In experiments where continuous coatings form, the silicate glass is no longer directly
19 exposed to the gas after the initial formation of the sulfate coating. Ongoing reaction requires a
20 transport mechanism through the coating. Consequently, there are three possible growth pathways.
21 First, if the reactive gas diffuses very fast through the sulfate, the reaction occurs at the interface
22 between the sulfate and the silicate glass, below the coating. This type of mechanism commonly
23 occurs during the oxidation of metals, where oxygen migrates through the oxide coating to the
24 interface between the coating and the pristine metal (Evans et al. 1983). If a similar mechanism
25 operates in $\text{SO}_{2(g)}$ -substrate reactions we would expect a continuous outward displacement of the
26 previously formed sulfate. Such an outward expansion would result in cracks in the coating around
27 edges of the silicate glasses, which are not observed in any experiment. Second, if the cations
28 diffuse rapidly through the coating, growth would occur at the surface interface between the sulfate
29 and the gas. In this case growth would occur continuously across the surface and deformation of
30 the coating would be avoided. This texture has not been observed in any experiments recorded in
31 the literature. In a third possible mechanism, cations and the gas phase migrate at a comparable
32 rate through the sulfate layer. In this case the reaction and growth occur within the sulfate coating,
33 most easily at grain boundaries (Fig. 4c). This growth mechanism results in the accumulation of
34 stress in the coating. The dissipation of this stress results in three different possible deformation
35 textures (Fig. 5). First, because transport of cations and $\text{SO}_{2(g)}$ most easily occurs along grain
36 boundaries (Fig. 4c), newly-formed sulfate would accumulate at grain boundaries preferentially
37 (Fig. 5d). This epitactic overgrowth would continue to such an extent that it results in the formation
38 of protrusions such as whiskers and hillocks. These features are indicated in Figure 5a for a reacted
39 eutectic An-Di glass. The formation of whiskers and hillocks extending from coatings is also
40 observed in thin film materials where strain is localized, and the growth of materials is focused
41 outwards by diffusive transport. For example, tin whiskers are commonly observed growing out of
42 intermetallic coatings (Sobiech et al. 2009; Chason et al. 2013). Second, where grains extend
43 laterally and stress is not focused on a small area, individual sulfate crystals can be bent upwards
44 at grain boundaries to form a chicken-wire texture (Fig. 5b and e) (Tolpygo and Clarke 1998b;
45 Clarke 2003). Third, entire polycrystalline sulfate layers can wrinkle and buckle due to internal
46 stress and expansion (Fig. 5c and f). This type of texture occurs when the rate of growth is very
47 high (Clarke 2003). For example, such a coating is shown in Figure 5 with extensively deformed
48 buckles. Within experimental durations, the volume between the buckled coatings and the substrate
49 is not infilled with additional sulfate material, although this may occur over much longer durations.
50 Similar deformation processes resulting in buckled coatings are observed in oxide coatings formed
51 in gas-alloy reactions (Evans et al. 1983; Clarke 2003; Birks et al. 2006). The presence of diverse
52 deformation textures formed by continuous sulfate coatings on glasses reacted with $\text{SO}_{2(g)}$ (Fig. 5)

1 strongly implies that these coatings indeed grow internally as illustrated in the schematic drawing
2 in Figure 4c. Independent of the mechanisms by which the sulfates grow, the reaction results in a
3 volume increase in the run products. In natural sub-volcanic systems this may result in the filling
4 of veins as the gas passes through and reacts with the surrounding rocks (Henley et al. 2017).

5 In summary, in the case of continuous sulfate coatings $\text{SO}_{2(g)}$ and cations need to migrate
6 into the sulfate coating, where new sulfate forms preferentially at grain boundaries (Fig. 4). This
7 process results in an increase of the coating volume and commonly causes deformation in the
8 coating. Deformation textures observed in experiments include whiskers, chicken-wire textures,
9 and buckling and wrinkling of the coating (Fig. 5). The degree of deformation increases with
10 increasing amount of sulfate formed.

11 **Compositional changes in the Fe-free glass substrate**

12 The mineralogical investigation of the coatings formed by reactions of $\text{SO}_{2(g)}$ with Fe-free
13 silicate glasses has shown that Ca-sulfates are the dominant reaction products. The observed
14 variation of sulfate phases formed as a function of temperature and relative to the glass transition
15 temperature underlines the importance of the role of the substrate composition on the overall
16 reaction mechanism and reaction rates. For example, Renggli et al. (in prep.) have shown that
17 sulfate reaction products have mole% $\text{Ca}/(\text{Ca}+\text{Mg})$ that generally exceed the mole% $\text{Ca}/(\text{Ca}+\text{Mg})$
18 in the reactant anorthite-diopside glasses ($(\text{Ca}/(\text{Ca}+\text{Mg}))_{\text{diopside}} = 0.5$, $(\text{Ca}/(\text{Ca}+\text{Mg}))_{\text{anorthite}} = 1$). In
19 the anorthite-diopside system at 600 °C the sulfate reaction products are relatively enriched in Ca
20 by 20-40%. At 800 °C, above the glass transition temperatures of all An-Di glasses except for the
21 anorthite endmember, this fractionation effect is much stronger and only minor or trace amounts
22 of Mg are detected in the sulfate reaction products. The mole% $\text{Ca}/(\text{Ca}+\text{Mg})$ at 800 °C is near 1 in
23 the sulfate formed on all anorthite-diopside glasses (Renggli et al. in prep.). This means that Ca
24 preferentially moves out of the glass to form the sulfates and Mg is relatively retained in the glass,
25 as discussed further below.

26 The reaction of $\text{SO}_{2(g)}$ with a silicate glass requires the mobilization of alkali or alkaline
27 earth metals to form sulfates at the reaction interface. As the relative abundances of Ca and Mg in
28 the sulfate reaction products vary both with temperature relative to the glass transition and also
29 with the composition of the unreacted glasses diffusional transport mechanisms appear to be
30 important rate controlling factors. The reaction at the surface causes chemical potential gradients
31 which drive mass fluxes. As Ca moves to the surface, additional chemical potential gradients result
32 in the interior of the silicate requiring charge compensation which causes compositional and
33 structural changes, in some cases resulting in crystallization. If the diffusion of Ca is a rate limiting
34 factor of the overall reaction, then the rate of sulfate formation must also change with experimental
35 duration. This change in the diffusivities of sulfate forming cations with experimental duration is
36 very poorly constrained and requires future experimental work.

37 The loss of charge-compensating cations and network-modifying cations from the glass to
38 the surface may require charge balancing. In systems without multivalent elements available to
39 change the valence state to accommodate a change in the electrochemical environment, charge
40 balancing may occur via four different mechanisms. First, anions can co-diffuse with the outward
41 fluxing cations. Second, charge compensation can occur via the counter diffusion of electron holes.
42 Third, charge compensation can occur via the counter diffusion of negatively-charged sulfur.
43 Fourth, Al^{3+} may adapt its coordination and partially become a network-modifier with five- and
44 six-fold coordination (Neuville et al. 2006; Le Losq et al. 2014). There is much work to be done to
45 demonstrate how these different charge balancing mechanisms behave in different materials.

46 Nucleation and growth of crystallites due to structural changes of the glass induce further
47 chemical potential gradients and affect the diffusivities of the diffusing cations. The interplay of
48 these processes during reactions of $\text{SO}_{2(g)}$ with the silicate surface can result in complex textures
49 that reflect the ongoing nature of the reactions and may result in phase assemblages which are out

1 of equilibrium, both in the surface coating and in the silicate. Crystallization in the substrate at the
2 surface, in Fe-free glasses, has only been observed at or near the glass transition temperature. It
3 has been documented in three experiments at 800 °C with diopside glass ($T_g = 722$ °C), $An_{15}Di_{85}$
4 glass ($T_g = 729$ °C) and $An_{48}Di_{52}$ glass ($T_g = 760$ °C), where diopside crystallized at the interface
5 (Renggli et al. in prep.). When crystallization occurs at the reaction interface the overall reaction
6 rate may be affected significantly and additional variables such as crystal structure, orientation and
7 grain size distribution require consideration in the future (see King et al. 2018).

8 $SO_{2(g)}$ REACTIONS WITH FE-BEARING GLASSES

9 Mineralogy of phases formed on Fe-bearing glass substrates

10 The reaction products formed on Fe-bearing glasses include $CaSO_4$, $MgSO_4$, Na_2SO_4 ,
11 $Na_2Ca(SO_4)_2$, K_2SO_4 , $Al_2(SO_4)_3$, $FeSO_4$, hematite, magnetite and Ti-bearing oxides (Table 2).
12 These phases have been determined by a range of direct and indirect methods including SEM,
13 Raman spectroscopy, X-ray photoelectron spectroscopy (XPS), Fourier transform infrared
14 spectroscopy (FTIR), X-ray diffraction (XRD), transmission electron microscopy (TEM),
15 nanoSIMS and leachate solution analysis (Johnson and Burnett 1993; Burnett et al. 1997; Li et al.
16 2011; Ayris et al. 2013). Examples of these analyses are described in more detail in Dalby et al.
17 (2018, this volume) and Palm et al. (2018, this volume).

18 Early experiments between $SO_{2(g)}$ and Fe-bearing glasses provided variable of results, in
19 part due to Equation (2) listed above. Johnson and Burnett (1993) used a 1:1 mixture of $SO_{2(g)}$ and
20 $O_{2(g)}$ that likely formed $SO_{3(g)}$ (Equation (2)) compared to pure $SO_{2(g)}$ in a sealed silica tube used
21 by Burnett et al. (1997). In the first case, the reaction products include a large range of different
22 sulfates (Ca, Mg, Na, K, Fe and Al) in all three experiments, as summarized in Table 2.

23 The studies by Johnson and Burnett (1993) and Burnett et al. (1997) used the same glasses
24 for their experiments, including a chondrule glass, obsidian and Kilauea basalt (Table 2). As
25 described above, the presence of K-sulfate in some experiments by Johnson and Burnett (1993) is
26 likely due to reaction with K from the starting $K_2S_2O_8$ used to produce the gas phase. Burnett et al
27 (1997) were able to demonstrate the presence of reduced sulfur using photoelectron spectroscopy
28 (XPS) on experimental products of disproportionation reactions with pure $SO_{2(g)}$, but the sulfide
29 phases were not directly determined. The experiments using pure $SO_{2(g)}$ resulted in significantly
30 smaller amounts of reaction products, with $CaSO_4$ on the chondrule glass, very small amounts of
31 Fe-sulfate on the obsidian and no detected reaction products on the Kilauea basalt (Burnett et al.
32 1997).

33 Ayris et al. (2013) used a gas mixture which is closer to a naturally occurring mixture in
34 explosive volcanic eruptions, consisting of a small quantity of $SO_{2(g)}$, air and $He_{(g)}$. They used glass
35 substrates with tephrite, phonolite, dacite, and rhyolite compositions. In the 600-800 °C range,
36 $CaSO_4$ is the only phase observed on the surface of any of the glasses (Ayris 2010; Ayris et al.
37 2013) (Table 2). At 300-600 °C, there was no detected reaction on the rhyolite glass yet the other
38 glasses were coated with $CaSO_4$ and the tephrite glass also had minor amounts of Na_2SO_4 . In the
39 0-300 °C range no reaction products were detected on any of the tested glass compositions after
40 one hour.

41 On natural glasses, these authors found that the initial rates of reaction are very high, with
42 sulfate detected by leachate analysis on the glass surfaces at 800 °C within 30 seconds. This high
43 rate of $SO_{2(g)}$ uptake in the first minute is due to fast adsorption onto the surface. This is followed
44 by lower reaction rates, which are controlled by diffusive transport of Ca^{2+} from the interior of the
45 glass to the surface. Overall, the amount of reaction increases with the Ca-concentration in the
46 glass (Ayris et al. 2013). The textures observed by Ayris et al. (2013) on glasses reacted at 800 °C
47 for 1 hour show discontinuously distributed, faceted $CaSO_4$ crystals with diameters ranging from
48 few hundred nanometers to 5 μm . The textures are comparable to those observed on soda-lime,

1 albite and diopside glass (see Fig. 2 and 3; Burnett et al. 1997). The texture in Figure 2 also
2 underlines the importance of polishing the glass surface exposed to the reacting gas. The presence
3 of a scratch results in an increasing degree of nucleation and formation of sulfate (Fig. 2; Burnett
4 et al 1997).

5 Li et al. (2010) used the same experimental setup as Johnson and Burnett (1993),
6 conducting experiments with crystalline basalts. At 600 °C they observed CaSO₄, whereas at
7 850 °C they observed an assemblage of CaSO₄, MgSO₄ and Fe₂O₃ (Li et al. 2010). Similar multi-
8 phase assemblages were observed on basalt glasses reacted with SO_{2(g)} (Table 2).

9 CaSO₄ and Na₂SO₄ and Fe₂O₃ were the major products with lesser MgSO₄, Fe₃O₄ and Fe-
10 Ti-oxides, in the case of both tholeiitic basalt glasses at 700 °C for 1 hour and 24 hours, and alkali
11 basalt glass at 800 °C for 1 hour (Table 2). These tholeiitic basaltic glasses included a series where
12 the Fe³⁺/Fe²⁺ was set at a range of values by pre-equilibrating the melt at different *f*O₂ conditions
13 (Dufresne et al. 2015). The unreacted glasses had molar Fe³⁺/Fe²⁺ = 0.08 (pre-equilibrated 1.5 log-
14 units in *f*O₂ below the Ni-NiO buffer (NNO-1.5)) to 0.54 at one log-unit in *f*O₂ above the Ni-NiO
15 buffer (NNO+1) (Dufresne et al. 2015).

16 The coating mineral assemblages depend on the Fe³⁺/Fe²⁺ ratios in the unreacted glasses,
17 the temperature and the experimental duration. Examples of the textures formed at 700 °C under a
18 stream of SO_{2(g)} for 24 hours are shown in Figure 6. In all three examples, CaSO₄ is the predominant
19 sulfate phase in the coatings. The glass pre-equilibrated at NNO-1.5 is continuously coated with a
20 mixture of Ca- and Mg-sulfate and very small sub-micron Fe-oxides. In the short experiment of 1
21 hour, the coating also included some Na₂SO₄. Glasses pre-equilibrated at NNO and NNO+1 show
22 large CaSO₄ crystals with lengths of up to 100 μm (Fig. 6). The coating on the glass pre-
23 equilibrated at NNO further includes dark areas of MgSO₄, smaller amounts of Na₂SO₄ and Fe₂O₃
24 in between the CaSO₄ crystals. At NNO+1 the coating includes a fine-grained mixture of Na₂SO₄
25 and micron-sized hematite crystals (Fig. 6c). Larger oxide crystals also occur, including some Fe-
26 Ti-oxides on the CaSO₄ crystals and minor amounts of Al in some Fe-Ti-oxide grains (Fig. 6).
27 Small grains of MgSO₄ were observed on the NNO+1 sample after 1 hour, whereas no MgSO₄ was
28 detected after 24 hours.

29 In addition to Fe₂O₃ the more reduced magnetite (Fe₃O₄) mineral has been observed in the
30 coatings of basalt glasses pre-equilibrated at the iron-wüstite redox buffer (Palm et al. 2018). The
31 dominant sulfate phase in these experiments is Na₂Ca(SO₄)₂ (glauberite) with significant amounts
32 of CaSO₄. The results from these experiments reacting basalt at 800 °C are described in detail as a
33 case study in the chapter by Palm et al. (2018, this volume).

34 In summary, phase assemblages of the coatings formed by the reaction of SO_{2(g)} with Fe-
35 bearing basalt glasses vary as a function of the composition and the Fe³⁺/Fe_{total} of the glass prior to
36 the reaction with SO_{2(g)} (Table 2). The sulfates observed in the coatings are CaSO₄, MgSO₄, Na₂SO₄
37 and Na₂Ca(SO₄)₂. The oxides observed in the coatings are hematite, magnetite and Ti-bearing
38 oxides. Future work will be required to determine the mechanisms which control the phases formed
39 in SO_{2(g)} reactions with Fe-bearing basalt glasses.

40 **Textures of sulfate coatings on Fe-bearing glass substrates**

41 All experiments produced by reacting SO_{2(g)} with Fe-bearing glasses have discontinuous
42 coatings (Fig. 6, Burnett et al. 1997; Ayris et al. 2013). After one hour at 700 °C the coatings cover
43 up to 80% of the surface area of the glass. The coverage increases with time reaching more than
44 90% after 24 hours. The texture of the sulfate-coating on the tholeiitic basalt pre-equilibrated at
45 NNO-1.5 reacted at 700 °C for 24 hours (Fig. 6a) is very similar to that on the Fe-free basalt reacted
46 at the same temperature and for the same amount of time (Fig. 4b). Both figures show backscattered
47 electron images with similar well-crystallized CaSO₄ grains with sub- and anhedral Mg-sulfates
48 which partly hydrated after the experiments. Only a few gaps occur in the coatings, exposing the

1 substrate and they are usually surrounded by CaSO₄ crystals (Fig. 6a). The CaSO₄ have diameters
2 of less than 2.5 μm.

3 The coatings on the more oxidized basalts (NNO and NNO+1) reacted at 700 °C for 1 hour
4 and 24 hours share the feature of well crystallized large euhedral anhydrite grains. The large
5 anhydrite grains usually show a distinct cleavage perpendicular to the longest axis of the grains.
6 As anhydrite has the best cleavage in the (001)-plane (Tröger 2017), the longest axis of the grains
7 in the coatings are the crystallographic c-axis of anhydrite (Fig. 6).

8 After one hour, Mg- and Na-sulfates form very fine-grained textures, with grain-sizes of
9 few microns on the glasses pre-equilibrated at NNO and NNO+1. The Mg-sulfates form equant
10 shaped grains, whereas the Na-sulfates have needle-shaped habits which are commonly twinned.
11 The Na-sulfates usually occur as patches surrounding elongated CaSO₄ grains. The metal oxides
12 are most frequently found lining the edges of these sulfate patches.

13 After 24 hours the CaSO₄ grains are up to five times larger compared to coatings on 1-hour
14 experiments. Individual crystals of CaSO₄ are no longer isolated and there are gaps in-between
15 crystals which are largely filled by other phases. On the glass pre-equilibrated at NNO, Mg-sulfate
16 (where present) occurs in large patches which partially overgrow and surround the CaSO₄ grains.
17 The Na₂SO₄ lines the edges of the CaSO₄ grains. In this coating, metal oxides reach grain sizes of
18 more than 20 μm (Fig. 6b). In the coating formed on the most oxidized glass (NNO+1) Na₂SO₄
19 patches tend to overgrow the CaSO₄ grains (Fig. 6c). The metal oxides are either found as micron-
20 sized needles in the Na₂SO₄ patches, or as large Fe-oxides (commonly Ti-bearing) between sulfates
21 and on top of large CaSO₄ grains.

22 In comparison with the textures observed on Fe-free glasses, the coatings formed by
23 reactions between SO_{2(g)} and Fe-bearing glasses are significantly different. CaSO₄ is the dominant
24 phase in most Fe-bearing and Fe-free systems, but the grain morphologies and sizes are very
25 different. On Fe-bearing glasses, CaSO₄ forms large grains with diameters of up to tens of microns
26 (Fig. 2, Fig. 6), whereas on Fe-free glasses CaSO₄ usually forms continuous coatings with small
27 grain sizes of up to several microns (Fig. 4, Fig. 5). The large CaSO₄ grains in coatings on Fe-
28 bearing glasses are, in some cases, associated with various other phases including sulfates and
29 oxides (Fig. 6), whereas in other cases CaSO₄ remains the only phase detected in the coatings
30 (Table 2, Ayris et al. 2013). This diversity of textures and assemblages shows that more work is
31 needed to constrain the processes which control the textures and assemblages formed in reactions
32 between SO_{2(g)} and Fe-bearing aluminosilicate glasses.

33 **Compositional changes in the Fe-bearing glass substrate**

34 Reaction products are also found in the glass substrate in layers or dispersed near the
35 interface with the gas and sulfate coating. For example, chondrule glass substrates produced a
36 region rich in silica and a Na-Ca-Mg-Al silicate, possibly clinopyroxene, in the glass below the
37 CaSO₄ coating (Johnson and Burnett 1993; Burnett et al. 1997). Ayris et al. (2013) used
38 transmission electron microscopy energy-dispersive X-ray spectroscopy (TEM-EDS) to show that
39 the reacted tephrite (Fig. 2) and phonolite glasses are depleted in Ca near the surface. This depletion
40 supports the assumption that Ca diffusion in the glass is the rate controlling step in the sulfate
41 forming reaction. The cross-section of the tephrite glass shows the nanometer scale nucleation of
42 a silicate phase, identified as the clinopyroxene augite by X-ray diffraction (Ayris et al. 2013).
43 Palm et al. (2018, this volume) also observed the crystallization of clinopyroxene in an alkaline
44 basalt glass reacted with SO_{2(g)} at 800 °C.

45 Reactions between tholeiitic basalt glasses and SO_{2(g)} record considerable complexity in
46 these non-equilibrium reactions. For example, a cross-section through the sulfate-rich coating on a
47 tholeiitic basalt glass, pre-equilibrated at the NNO buffer is shown in Figure 7. The images are
48 maps of major elements obtained by nanoscale secondary ion mass spectrometry (nano-SIMS, see
49 Palm et al. 2018, this volume). The network-forming cations Si and Ti show small or negligible

1 concentration gradients across the interface from the coating into the glass. In some instances, SiO₂
2 needles form in the reacted glass substrate near the surface. Magnesium and Fe are strongly
3 depleted within the outermost two microns of the glass and show an increase within 20 μm of the
4 surface. The degree of nucleation of Mg- and Fe-rich phases varies considerably between the
5 experiments although consistently crystallization occurs along a gradient of increasing crystal
6 density towards the reaction surface (Fig. 7). The main sulfate-forming cation is Ca, as reflected
7 by a high relative count rate in the surface layer. The glass substrate is accordingly depleted in Ca.
8 Sodium shows a very different behavior because it partitions into the sulfate coating, but is also
9 enriched in the near-surface silicate substrate (Fig. 7).

10 DISCUSSION

11 In this section, we discuss the reaction mechanisms and possible rate-limiting steps in gas-
12 glass reactions. Since Ayris et al. (2013) found that reactions were most efficient above 600 °C, we
13 focus the discussion on experiments in the temperature range of 600-800 °C. First, we discuss the
14 observation from experiments with Fe-free aluminosilicate glasses. Second, we discuss Fe-bearing
15 systems, in which redox reactions play an important role. For this reason, we will examine the
16 variables SO_{2(g)} and O_{2(g)} and their effect on the reaction products in the coatings and the altered
17 glass substrates.

18 In all experiments recorded in the literature, in which SO_{2(g)} was reacted with Ca-, Mg- and
19 Na-bearing aluminosilicate glasses, the sulfate reaction products are relatively enriched in Ca
20 relative to the unreacted bulk glass composition, hence Ca migrates out of the glass more than Mg.
21 This is the case for both Fe-bearing and Fe-free systems. As pointed out, the sulfates almost entirely
22 consist of CaSO₄ on An-Di glasses reacted at 800 °C, whereas at 600 °C some MgSO₄ is present.
23 CaSO₄ has lower Gibbs free energies of formation than MgSO₄ from 25 °C to >1500 °C, making it
24 a more stable phase. At 600 °C calculated Gibbs free energies of formation are -1558.7 kJ/mol for
25 CaSO₄ and -1372.3 kJ/mol for MgSO₄, and at 800 °C they are -1608.5 kJ/mol for CaSO₄ and -
26 1418.1 kJ/mol for MgSO₄ (Chase 1998). The differences in the Gibbs free energies of formation
27 are -186.4 kJ/mol at 600 °C and -190.4 kJ/mol at 800 °C. These data show that CaSO₄ is
28 thermodynamically more stable than MgSO₄, but the presence of MgSO₄ at 600 °C, and not at 800
29 °C, cannot be ascribed to the thermodynamic properties. Thermodynamic properties of the sulfates
30 are discussed in more detail in King et al. (2018, this volume) and applied to reactions in planetary
31 environments and on Venus in Zolotov (2018, this volume).

32 If the rate limiting factor is diffusion in the glass substrate, supplying cations to the surface for the
33 formation of sulfate, we can expect that the cation with the larger diffusion coefficient is relatively
34 more abundant in the sulfate reaction products. To our knowledge there is no data on the
35 diffusivities of Ca and Mg in anorthite-diopside glasses, but in albite and jadeite glasses at 800 °C
36 the tracer diffusivities of the cations follow the order of $D_{Na} > D_{Ca} > D_{Mg}$ (Roselieb and Jambon,
37 2002). The same relationship likely holds for the compositionally similar anorthite-diopside glasses
38 and diffusivities in the glass follow $D_{Ca^{2+}}^{glass} > D_{Mg^{2+}}^{glass}$. The enrichment of Ca in the sulfate compared
39 to Mg appears to depend on the temperature, relative to the glass transition, with a higher mobility
40 for Ca than Mg (Renggli et al. in prep.). This suggests that the substrate properties control the
41 supply of cations and the amount of reaction products formed. Further work is needed to unravel
42 the relative mobilities of the sulfate forming cations as a function of temperature, composition and
43 properties of the reactants.

44 We posit that network-modifying cations which are not charge-compensating are the most
45 easily mobilized as a function of temperature or due to chemical potential gradients, as imposed by
46 gradients in gas-solid and redox reactions. In the absence of systematic studies on the relative
47 diffusivities of Ca and Mg in aluminosilicate glasses we draw on our experimental results. The
48 high relative mobility of Ca indicates that it is less strongly bound in the glass aluminosilicate
49 network than Mg, or that it is more readily mobilized by reaction with SO_{2(g)}. This distinction may

1 be explained by the difference in the ionic field strengths of the cations. The ionic field strength is
2 the ratio of the valence of the cation over the squared effective ionic radius for a given coordination
3 number. The calculated ionic field strengths for 6-fold oxygen coordinations are 3.86 for Mg and
4 2 for Ca (Shannon 1976), which suggests that Mg may form stronger bonds with non-bridging
5 oxygens, and is more likely to be retained in the glass to charge compensate Al^{3+} and Fe^{3+} cations.
6 This interpretation remains speculative and will require further experimental work on simple
7 glasses in the future.

8 **Role of the fugacities of $\text{SO}_{2(g)}$ and $\text{O}_{2(g)}$ on reactions with silicate glasses**

9 The reaction between $\text{SO}_{2(g)}$ and silicate glasses is thermodynamically expected to form
10 sulfates and sulfides due to the disproportionation of S^{4+} in the gas molecule to S^{6+} in the sulfate
11 and S^{2-} in a sulfide or gas phase (Equation (4)). However, the description of the experimental
12 reaction products from a range of different studies has shown that sulfides are rarely observed (only
13 with XPS), both in Fe-free and Fe-bearing systems. Fe occurs in hematite in experiments with
14 tholeiitic basalts (Fig. 6), thus a high oxygen fugacity seems to be a plausible mechanism,
15 prohibiting the formation of sulfides. If the reacting $\text{SO}_{2(g)}$ is in equilibrium, the speciation
16 calculation shown in Figure 1 can be used to establish the oxygen fugacity ($f\text{O}_2$) of the gas phase
17 ($\log f\text{O}_2 = -12.1$ at $700\text{ }^\circ\text{C}$), assuming that the gases mix in an ideal manner. This calculated value
18 is uncertain due to high gas flow rates (up to 50 standard cm^3 per minute) which likely ensures that
19 $\text{SO}_{2(g)}$ remains the dominant species and $\log f\text{O}_2$ may be lower. Second, the zone in the furnace at
20 which the experimental temperature of $700\text{ }^\circ\text{C}$ is reached is small, so that equilibrium in the gas is
21 unlikely.

22 Understanding the $f\text{O}_2$ in Fe-bearing experiments is of importance because this variable
23 controls the stability of different Fe-oxide phases. The phase relationship in the system Fe-S-O
24 is commonly shown as a function of $f\text{O}_2$ and $f\text{S}_2$ (Hall 1986). Here instead we calculate the phase
25 relations using thermodynamic data (Chase 1998) to recast the relationship as a function of $f\text{SO}_2$
26 and $f\text{O}_{2(g)}$ (Fig. 8). It should be noted that the thermodynamic calculations assume activities of unity
27 in both the reactant and the product. This is not the case and results in uncertainties in applying the
28 experimental results to the calculated phase boundaries.

29 The Ni-NiO $f\text{O}_2$ -buffer (NNO) is shown in Figure 8, at $\log f\text{O}_2 = -16.3$ (O'Neill and
30 Pownceby 1993). This is 4.7 orders of magnitude below the $f\text{O}_2$ of the calculated magnetite-
31 hematite buffer above which the oxides are placed in the coatings of the reacted tholeiitic basalt
32 glasses pre-equilibrated near NNO (Fig. 8). An even greater overall oxidation is required in the
33 reaction of $\text{SO}_{2(g)}$ with alkali basalt glasses pre-equilibrated at the iron-wüstite buffer, where both
34 magnetite and hematite were observed in the coatings (see Palm et al. 2018). Therefore, $\text{SO}_{2(g)}$
35 reactions with Fe-bearing silicate glasses are characterized by chemical potential gradients imposed
36 by the sulfate-forming reaction (Equation (4)) and by redox reactions (Fig. 8). This combination in
37 gradients creates a system which is highly out of equilibrium, forcing the reaction to be more
38 effective.

39 Burnett et al. (1997) were the only authors who reported the observation of Fe-sulfate, on
40 an obsidian sample reacted with $\text{SO}_{2(g)}$ at $850\text{ }^\circ\text{C}$, based on XPS spectra and optical microscopy.
41 In a reaction with pure $\text{SO}_{2(g)}$ Fe-sulfates are not predicted thermodynamically (Fig. 8). Overall,
42 the reaction with obsidian produced very small amounts of reaction product on the surface, likely
43 due to the low concentrations of Na_2O (3.80 wt.%), CaO (0.52 wt.%) and FeO (1.02 wt.%), and
44 the high concentrations of Al_2O_3 (12.32 wt.%) and SiO_2 (76.45 wt.%) (Burnett et al. 1997). As
45 traces of the same Fe-bearing phase were observed in an Fe-free experiment with an Ab-An-Di
46 glass, where the observation was interpreted as a contamination (Burnett et al. 1997), the same
47 contamination may also explain the observation on the obsidian sample.

48 Iron is the most abundant multivalent cation in natural aluminosilicates. In glasses and
49 melts the redox state of iron affects its coordination state in the amorphous network and physical

1 properties including viscosity and liquidus temperatures (Farges et al. 2004; Wilke 2005). As
 2 indicated above, $\text{SO}_{2(\text{g})}$ reactions with Fe-bearing aluminosilicate glasses result in the formation of
 3 Fe-oxides in the coatings and also affect the redox state of Fe in the glass substrates. With ongoing
 4 reaction physical properties of the glasses affected by the redox state of iron are expected to change
 5 accordingly. Therefore, it is important to investigate the mechanism of oxidation here.

6 The oxidation of Fe^{2+} in a silicate melt or glass may occur via several different kinetic
 7 pathways. The pathway which reduces the chemical potential gradient of oxygen the fastest is the
 8 dominant mechanism for Fe^{2+} oxidation. In hydrogen-bearing systems the diffusion rate of free H_2
 9 is very high. The hydrogen is bound in the form OH-groups following the oxidation reaction of
 10 ferrous to ferric iron (Gaillard et al. 2003). When studying reactions between gases and Fe-bearing
 11 glasses it is therefore important to determine if hydrogen is present in the system, as it can
 12 significantly affect redox reactions.

13 In a hydrogen-free system, three redox pathways are possible. First, molecular O_2 may
 14 diffuse through the glass to increase the cation/oxygen ratio, or ionic O^{2-} and charge-compensating
 15 electron holes can co-diffuse to decrease the chemical potential gradient (Magnien et al. 2008;
 16 Wendlandt 1991). In both cases the cation/oxygen ratio changes in response to the redox gradient.
 17 Second, divalent and monovalent cations move to the surface, balanced by the counter-diffusion
 18 of electron holes (h') (Fig. 9b) (Magnien et al. 2008). It has been shown that molecular and ionic
 19 oxygen diffusion is very slow in super-cooled melts and aluminosilicate glasses (Cook et al. 1990;
 20 Cooper et al. 1996b, a; Magnien et al. 2008; Cochain et al. 2013). For example, there is negligible
 21 uptake of atmospheric oxygen by oxidizing and reheating Kilauea basalt glasses at temperatures
 22 below 1200 °C (Burkhard 2001). The third pathway dominates when the diffusivities (D) of
 23 monovalent/divalent cations and electron holes are considerably faster than the diffusivities of
 24 molecular and ionic oxygen, and if the system is hydrogen-free (subscripts denote diffusing
 25 species):

$$26 \quad D_{\text{O}_2}, D_{\text{O}^{2-}} \ll D_{\text{M}^+}, D_{\text{M}^{2+}} \ll D_{h'}. \quad (5)$$

27 In the case of oxidation of crystalline oxides, for which the same principle of cation
 28 diffusion is valid, the diffusion of monovalent and divalent cations to the surface is charge-balanced
 29 by the inward diffusion of cation vacancies, particularly along dislocations (Schmalzried 1983;
 30 Ostyn et al. 1984; Schmalzried and Backhaus-Ricoult 1993). In crystalline materials electron holes
 31 are the equivalent of Fe^{3+} cations occupying the sites of Fe^{2+} cations (Cooper et al. 1996a).

32 In aluminosilicate glasses with multivalent transition metals electron holes are mobile. For
 33 example, Fe^{2+} easily releases an electron, or in other words takes up an electron hole. The material
 34 behaves like a semiconductor for electron holes, as they can jump between transition metals almost
 35 instantaneously (Cooper et al. 1996a; Cook and Cooper 2000). Due to this high mobility, electron
 36 holes do not create an electrochemical potential gradient and their flux is not rate limiting. The
 37 chemical potential gradient of oxygen from the surface to the interior results in the flux of
 38 monovalent and divalent cations to the surface, expressed as:

$$39 \quad j_{\text{M}^{2+}} = \frac{c_{\text{M}^{2+}} D_{\text{M}^{2+}}}{2RT} \cdot \frac{d\mu_{\text{O}_2}}{d\xi} \quad (6)$$

40 where $j_{\text{M}^{2+}}$ is the flux of divalent cations to the surface, $c_{\text{M}^{2+}}$ is its concentration, $D_{\text{M}^{2+}}$ is the self-
 41 diffusion coefficient, R is the gas constant, T is temperature in K and $\frac{d\mu_{\text{O}_2}}{d\xi}$ is the chemical potential
 42 gradient of oxygen with ξ being the distance variable (Cooper et al. 1996a; Cook and Cooper 2000).
 43 This relationship is fundamental for the oxidation mechanism, and shows the dependence of cation
 44 diffusion on the chemical potential gradient of oxygen (Cooper et al. 1996a; Cook and Cooper
 45 2000). As the major element abundance in the oxidizing surface layer is changed by the loss of
 46 cations to the surface, the physical properties of the silicate change also. Consequently, the
 47 diffusion coefficients are not constant with time (Schmalzried 1983).

1 A significant property of the reaction morphology of the oxidation of silicate glasses and
 2 super-cooled melts is the nucleation of oxides between the surface and the oxidation front if
 3 tetrahedrally coordinated Fe³⁺ is not sufficiently charge compensated (Fig. 9b; Cook et al. 1990;
 4 Cooper et al. 1996b; Cook and Cooper 2000). If, for example, sufficient Na is available as a charge
 5 compensator, nucleation of oxides in the glass is avoided. This is observed as an enrichment of Na
 6 in the oxidized glass layer. In this case, the oxidation front coincides with a Na-front (Cook et al.
 7 1990; Cook and Cooper 2000; Burkhard 2001). In the absence of sufficient charge compensating
 8 alkalis the glass structure is no longer stable and oxides nucleate homogeneously (Cooper et al.
 9 1996b, a; Cook and Cooper 2000). The nanoSIMS maps (Fig. 7) of a cross section through a
 10 tholeiitic basaltic glass pre-equilibrated at the NNO oxide buffer and reacted for 24 hours at 700
 11 °C show such an enrichment of Na near the surface in the glass substrate. The Na enrichment was
 12 not sufficient to charge-balance the oxidizing and reacting glass, which resulted in the nucleation
 13 of Fe-rich spherulites, surrounded by Mg-rich phases (Fig. 7).

14 The reaction mechanism of SO_{2(g)} with Fe-bearing silicate glasses and supercooled melts
 15 is comparable with that of oxidation. In both cases divalent cations diffuse to the surface due to a
 16 chemical potential gradient (Fig. 9). In the case of the SO_{2(g)} reaction (Figure 9a) gradients in fSO₂,
 17 fS₂ and other gas species (see Fig. 1) occur in addition to a gradient in fO₂. In the absence of S-
 18 bearing species diffusing divalent cations (Ca and Mg) form oxides near the surface (Cooper et al.
 19 1996a; Cook and Cooper 2000). In the presence of SO_{2(g)} the cations react to form sulfates and
 20 oxides. Due to the high fSO₂ of the experimental gas (Fig. 1 and 8) it is likely that the cation
 21 diffusion is predominantly due to the driving force of the reaction in equation (3) and only
 22 secondarily due to the effect of oxidation as described by Cooper et al. (1996a). The relative
 23 importance of these mechanisms remains to be determined experimentally.

24 **Reaction rates**

25 The depletion of cations in the glass substrate, due to the formation of sulfates and oxides
 26 on the surface, can result in the destabilization of the glass, resulting in the nucleation and
 27 crystallization of oxide and silicate phases (Fig. 4 and 9). Crystal growth can impose additional
 28 chemical potential gradients and affect the mobility of cations in the glass and their availability to
 29 form surface coatings. Crystallization near the surface can also act as a barrier for further diffusion
 30 of cations to the surface, and thus become reaction limiting.

31 The rate at which the reaction between SO_{2(g)} or O_{2(g)} with a glass occurs can be described
 32 by three different rate laws, depending on which mechanism is rate-limiting. First, if the surface
 33 reaction is rate limiting, then the law is linear and the rate is independent of time. This initial
 34 chemisorption reaction (Henley et al. 2015) is not likely the rate controlling mechanism because
 35 experimental work has shown that significant amounts of sulfate form almost instantaneously
 36 within few minutes (Ayrís et al. 2013). Second, if the reaction occurs at low temperature resulting
 37 in a very thin oxide layer, it follows a logarithmic law, which is not the case in high-temperature
 38 gas-solid reactions either. Third, if the reaction is diffusion controlled (Fig. 4 and 9) and the
 39 transport mechanisms are rate limiting, the rate follows a parabolic law and is inversely
 40 proportional to the square root of time (Birks et al. 2006):

$$41 \quad \frac{d\xi}{dt} = \frac{k'}{\xi} \quad (7)$$

42 Integrated:

$$43 \quad \xi = \sqrt{2k't} \quad (8)$$

44 where k' is the parabolic rate constant. The parabolic rate constant is an intrinsic property
 45 dependent on the cation flux, composition, concentration gradient, thermodynamic driving force
 46 and temperature and is derived experimentally (Pieraggi 1987; Cooper et al. 1996a; Monceau and
 47 Pieraggi 1998; Birks et al. 2006).

1 The rates of sulfate formation have been determined by leaching the coatings in solution
2 and measuring the concentration of the leached material as a function of the amounts of reacted
3 solids. Ayris et al. (2013) measured the molar amount of sulfur as a function of the weight of
4 reacted volcanic ash. After initial $\text{SO}_{2(\text{g})}$ adsorption, the formation of CaSO_4 is limited by the
5 diffusion of Ca from within the ash particles to the surface. Accordingly, they calculate a diffusion
6 coefficient for Ca^{2+} ($D_{\text{Ca}^{2+}}^{\text{glass}}$) assuming constant diffusion rates and solving Fick's first law of
7 diffusion for ideal spherical ash particles (Ayris et al. 2013). Diffusion rates are greatest in the
8 tephrite glass ($D_{\text{Ca}^{2+}}^{\text{tephrite gl.}} = 6.5 \times 10^{-14}$), followed by phonolite glass ($D_{\text{Ca}^{2+}}^{\text{phonolite gl.}} =$
9 1.8×10^{-12}), dacite glass ($D_{\text{Ca}^{2+}}^{\text{dacite gl.}} = 3.7 \times 10^{-13}$) and rhyolite glass ($D_{\text{Ca}^{2+}}^{\text{rhyolite gl.}} =$
10 8.7×10^{-13}). These diffusion coefficients apply to the first minutes of the reaction after $\text{SO}_{2(\text{g})}$
11 adsorbs onto Ca-O surface sites.

12 As the reaction proceeds, between $\text{SO}_{2(\text{g})}$ and silicate glasses, significant amounts of sulfate
13 can be formed. Consequently, the glasses become increasingly depleted in Ca, Mg or Na,
14 depending on the system. As the network-forming cations (Si, Al) are not extracted by the reaction,
15 the glass becomes increasingly Si- and Al-rich. This change in the chemical composition within
16 the near-surface glass affects the rates at which the divalent and monovalent cations can diffuse
17 and be extracted. For example, the rate of sulfate formation in reactions between $\text{SO}_{2(\text{g})}$ and silicate
18 glasses in the anorthite-diopside system is an order of magnitude higher within the first hour of
19 reaction compared to the following 23 hours (Renggli et al. in prep.). As pointed out in the context
20 of the oxidation of metal alloys (Schmalzried 1983), diffusion coefficients are not constant in these
21 systems and evolve with time. Furthermore, $\text{SO}_{2(\text{g})}$ -silicate glass reactions frequently result in the
22 nucleation of crystallites in the sub-surface glass. This has been observed in Fe-free and Fe-bearing
23 glass of a various compositions as indicated in Figures 4, 7 and 9 (Ayris et al. 2013, Renggli et al.
24 in prep.). It is for these reasons, that none of the rate laws, including parabolic rate laws,
25 sufficiently describe the reaction rates of $\text{SO}_{2(\text{g})}$ with silicate glasses. Future work needs to develop
26 kinetic models that encapsulate the complexity of the reaction mechanisms.

27 **Summary and outlook**

28 In summary, reactions between $\text{SO}_{2(\text{g})}$ and silicate glasses with diverse compositions have
29 been observed to form significant amounts of sulfate over short time frames of few minutes to an
30 hour at 600-800 °C (Ayris et al. 2013; Delmelle et al. 2018, this volume). In Ca-bearing systems,
31 the reaction products primarily consist of CaSO_4 coatings on the glass surfaces and associated Ca-
32 depleted glass substrates. In the presence of other di- and monovalent cations, in particular Na and
33 Mg, Ca remains the main sulfate forming cation. Other sulfates, including MgSO_4 , Na_2SO_4 and
34 $\text{Na}_2\text{Ca}(\text{SO}_4)_2$ have been observed in some experiments, but they usually occur in lesser abundance
35 than CaSO_4 . Experimental studies with natural volcanic ash samples, synthetic Fe-free glasses and
36 natural Fe-bearing glasses collectively suggest that the reaction rates and compositions of the
37 reaction products are a function of the physical properties of the reacting glasses, and in particular
38 the mobility of different cations in the glasses. In Al^{3+} - and Fe^{3+} -bearing systems some monovalent
39 and divalent cations are preferentially retained in the glass to charge-balance the tetrahedrally
40 coordinated Al^{3+} and Fe^{3+} . Calcium appears to be less strongly bound to the amorphous network
41 than Mg and Na, and is more easily mobilized to form CaSO_4 coatings. The reactions are further
42 complicated where $\text{Fe}^{3+}_{\text{tot}}$ increases (Fe^{2+} is oxidized to Fe^{3+}) with time due to oxidation, gradually
43 requiring more charge compensation.

44 The complexities underline the importance of future experimental investigations. In
45 particular, reaction rates at different stages of the reaction remain under-determined. Another open
46 question relates to what physicochemical properties and mechanisms control the mobility or
47 retention of alkali and alkaline earth metals in the aluminosilicate glasses. Recently, Le Losq et al.
48 (2017) have shown that percolation channels control the mobility of alkali metals in aluminosilicate
49 glasses and melts. Similar structural properties may also control the mobility of alkaline earth
50 metals in aluminosilicate glasses, and their transport to the surface to form sulfates as described in

1 this chapter. A better understanding of these structural properties is of fundamental importance for
2 the interpretation of reactions between aluminosilicate glasses and reactive gas species such as
3 $\text{SO}_{2(g)}$.

4 Experimental observations summarized in this chapter were all made at room temperature.
5 However, a number of these observations may be affected by the cooling paths of the samples at
6 the end of the experiments. For example, the nucleation of crystalline phases near the reacting
7 surface may occur during quench. Furthermore, some salts formed in these experiments can go
8 through phase transitions as they are cooled to lower temperatures (e.g. Na_2SO_4). Others such as
9 MgSO_4 are prone to hydration or may recrystallize at room temperatures. These mechanisms may
10 result in textural, mineralogical and chemical changes between experiment and analysis.
11 Experiments investigating gas-solid reactions *in situ* are therefore essential to better constrain these
12 secondary processes.

13 In systems which contain multivalent elements, in particular Fe, the oxygen fugacity is an
14 important variable. It varies in the glasses during the reactions, but also in the gas phase and in the
15 resulting coatings. Future interpretations would benefit from $f\text{O}_2$ monitoring during experiments
16 and the understanding of the reactions will improve with the determination of $\text{Fe}^{3+}/\text{Fe}^{2+}$ and $\text{S}^{6+}/\text{S}^{2-}$
17 across the reaction interface after the experiments, for example with XANES, which additionally
18 provides information about the coordination of Fe in the glasses (Wilke et al. 2007 and 2011).

19 ACKNOWLEDGMENTS

20 This work was supported by Australian Research Council funding to King
21 (DP150104604 and FT130101524). Renggli was supported by an ANU PhD scholarship.
22 We appreciate comments from Stephen Cox on the textural evolution of the surface
23 coatings. We thank Paul Ayris for providing the SEM image in Figure 2a. We thank Dave
24 Clark for assistance with the initial experiments. We thank Linda McMorro and Jill
25 Middleton for their help with sample analysis and Richard Henley and Andrew Palm for
26 fruitful discussions. The authors thank Paul Guagliardo for his assistance with nanoSIMS
27 and acknowledge the Australian Microscopy & Microanalysis Research Facility, AuScope,
28 the Science and Industry Endowment Fund, and the State Government of Western
29 Australia for contributing to the Ion Probe Facility at the University of Western Australia.
30 We acknowledge the use of the ANU Raman Facility in the Research School of Physics
31 and Engineering. The authors acknowledge the facilities, and the scientific and technical
32 assistance, of the Australian Microscopy and Microanalysis Research Facility at the Centre
33 of Advanced Microscopy, the Australian National University.

REFERENCES

- 1
2 Ayris PM (2010) High temperature SO₂ chemisorption on model systems. Implications for in-
3 plume processes. PhD thesis, University of York, York, UK
- 4 Ayris PM, Lee AF, Wilson K, Kueppers U, Dingwell DB, Delmelle P (2013) SO₂ sequestration in
5 large volcanic eruptions: High-temperature scavenging by tephra. *Geochim Cosmochim*
6 *Acta* 110:58–69, doi: 10.1016/j.gca.2013.02.018
- 7 Behrens H, Gaillard F (2006) Geochemical aspects of melts: volatiles and redox behavior.
8 *Elements* 2:275–280, doi: 10.2113/gselements.2.5.275
- 9 Behrens H, Stelling J (2011) Diffusion and redox reactions of sulfur in silicate melts. *Rev Mineral*
10 *Geochem* 73:79–111, doi: 10.2138/rmg.2011.73.4
- 11 Birks N, Meier GH, Pettit FS (2006) Introduction to the high-temperature oxidation of metals.
12 Cambridge University Press, Cambridge, UK; New York, 338pp
- 13 Burkhard DJM (2001) Crystallization and oxidation of Kilauea basalt glass: Processes during
14 reheating experiments. *J Petrol* 42:507–527, doi: 10.1093/petrology/42.3.507
- 15 Burnham CW (1979) Magmas and hydrothermal fluids. In *Geochemistry of Hydrothermal Ore*
16 *Deposits* (ed. Barnes HL) 71–136
- 17 Burnett DS, Goreva J, Epstein S, Haldemann SL, Johnson AR (1997) SO₂-rock interaction on Io.
18 Interaction with pure SO₂. *J Geophys Res Atmospheres* 102:19371–19382
- 19 Chase MW (1998) NIST-JANAF thermochemical tables, 4th edition. *J Phys Chem Ref Data*
20 *Monograph* 9, Am Chem Soc and Am Inst of Phys, Washington, DC, 1951pp
- 21 Chason E, Jadhav N, Pei F, Buchovecky E, Bower A (2013) Growth of whiskers from Sn surfaces:
22 Driving forces and growth mechanisms. *Prog Surf Sci* 88:103–131, doi:
23 10.1016/j.progsurf.2013.02.002
- 24 Clarke DR (2003) The lateral growth strain accompanying the formation of a thermally grown
25 oxide. *Acta Mater* 51:1393–1407, doi: 10.1016/S1359-6454(02)00532-3
- 26 Cochain B, Pinet O, Richet P (2013) Diffusion of sodium ions driven by charge compensation as
27 the rate-limiting step of internal redox reactions. *J Non-Cryst Solids* 365:23–26, doi:
28 10.1016/j.jnoncrystol.2013.01.016
- 29 Cook GB, Cooper RF (2000) Iron concentration and the physical processes of dynamic oxidation
30 in an alkaline earth aluminosilicate glass : *American Mineralogist*. *Am Mineral* 85:397–
31 406
- 32 Cook GB, Cooper RF, Wu T (1990) Chemical diffusion and crystalline nucleation during oxidation
33 of ferrous iron-bearing magnesium aluminosilicate glass. *J Non-Cryst Solids* 120:207–
34 222, doi: 10.1016/0022-3093(90)90205-Z
- 35 Cooper RF, Fanselow JB, Poker DB (1996a) The mechanism of oxidation of a basaltic glass:
36 Chemical diffusion of network-modifying cations. *Geochim Cosmochim Acta* 60:3253–
37 3265, doi: 10.1016/0016-7037(96)00160-3

- 1 Cooper RF, Fanselow JB, Weber JKR, Merkley DR, Poker DB (1996b) Dynamics of oxidation of
2 a Fe²⁺-bearing aluminosilicate (basaltic) melt. *Science* 274:1173–1176
- 3 Dalby K et al. (2018) Analytical techniques for probing gases and small-scale layers that preserve
4 information on gas-solid reactions. This volume
- 5 de Moor JM, Fischer TP, Sharp ZD, King PL, Wilke M, Botcharnikov, Cottrell E, Zelenski M,
6 Marty B, Klimm K, Rivard C, Ayalew D, Ramirez C, Kelley KA (2013) Sulfur degassing
7 at Erta Ale (Ethiopia) and Masaya (Nicaragua) volcanoes: Implications for degassing
8 processes and oxygen fugacities of basaltic systems. *Geochem Geophys Geosy* 14:4076–
9 4108
- 10 DePaolo DJ, Cole DR (2013) Geochemistry of geologic carbon sequestration: An overview. *Rev*
11 *Mineral Geochem* 77:1–14, doi: 10.2138/rmg.2013.77.1
- 12 Dingwell DB (2006) Transport properties of magmas: diffusion and rheology. *Elements* 2:281–
13 286
- 14 Dingwell DB (1990) Effects of structural relaxation on cationic tracer diffusion in silicate melts.
15 *Chem Geol* 82:209–216, doi: 10.1016/0009-2541(90)90082-I
- 16 Doute S (2002) Dynamics and evolution of SO₂ gas condensation around Prometheus-like volcanic
17 plumes on Io as seen by the near infrared mapping spectrometer. *Icarus* 158:460–482, doi:
18 10.1006/icar.2002.6889
- 19 Du H (2000) Thermodynamic assessment of the K₂SO₄-Na₂SO₄-MgSO₄-CaSO₄ system. *J Phase*
20 *Equilibria* 21:6–18, doi: 10.1361/105497100770340363
- 21 Dufresne CDM, King PL, Dyar MD, Dalby KN (2015) Effect of SiO₂, total FeO, Fe³⁺/Fe²⁺, and
22 alkali elements in basaltic glasses on mid-infrared. *Am Mineral* 94:1580–1590, doi:
23 10.2138/am.2009.3113
- 24 Evans AG, Crumley GB, Demaray RE (1983) On the mechanical behavior of brittle coatings and
25 layers. *Oxid Met* 20:193–216, doi: 10.1007/BF00656841
- 26 Farges F, Lefrère Y, Rossano S, Berthereau A, Calas G., Brown GE (2004) The effect of redox
27 state on the local structural environment of iron in silicate glasses: a combined XAFS
28 spectroscopy, molecular dynamics, and bond valence study. *J Non-Cryst Solids* 344:176–
29 188. Fegley B, Prinn RG (1989) Estimation of the rate of volcanism on Venus from reaction
30 rate measurements. *Nature* 337:55–58, doi: 10.1038/337055a0
- 31 Freyer D, Voigt W (2003) Crystallization and Phase Stability of CaSO₄ and CaSO₄ – Based Salts.
32 *Monatshefte für Chem Chem Mon* 134:693–719, doi: 10.1007/s00706-003-0590-3
- 33 Gaillard F, Scaillet B (2009) The sulfur content of volcanic gases on Mars. *Earth Planet Sci Lett*
34 279:34–43, doi: 10.1016/j.epsl.2008.12.028
- 35 Gaillard F, Schmidt B, Mackwell S, McCammon C (2003) Rate of hydrogen–iron redox exchange
36 in silicate melts and glasses. *Geochim Cosmochim Acta* 67:2427–2441
- 37 Gooding J (1978) Geochemical weathering on Mars: Thermodynamic stabilities of primary
38 minerals (and their alteration products) from mafic igneous rocks. *Icarus* 33:483–513
- 39 Hall AJ (1986) Pyrite-pyrrhotine redox reactions in nature. *Mineral Mag* 50:223–229

- 1 Henley RW, Hughes GO (2016) SO₂ flux and the thermal power of volcanic eruptions. *J Volcanol*
2 *Geotherm Res* 324:190–199, doi: 10.1016/j.jvolgeores.2016.04.024
- 3 Henley RW, King PL, Wykes JL, Renggli CJ, Brink FJ, Clark DA, Troitzsch U (2015) Porphyry
4 copper deposit formation by sub-volcanic sulphur dioxide flux and chemisorption. *Nat*
5 *Geosc* 8:210-215
- 6 Henley RW, Brink FJ, King PL, Clyde L, Ganguly J, Mernagh T, Middleton J, Renggli CJ, Sieber
7 M, Troitzsch U, Turner M (2017) High temperature gas-solid reactions in calc-silicate Cu-
8 Au skarn formation; Ertsberg, Papua Province, Indonesia. *Contrib Mineral Petr* 172:106–
9 125
- 10 Henley RW, Seward T (2018) Gas-solid reactions and reactive mass transport in volcanic systems.
11 *Rev Mineral Geochem* XX:xxx-xxx
- 12 Hsueh CH, Evans AG (1983) Oxidation induced stresses and some effects on the behavior of oxide
13 films. *J Appl Phys* 54:6672–6686, doi: 10.1063/1.331854
- 14 Hu R, Seager S, Bains W (2013) Photochemistry in terrestrial exoplanet atmospheres. II. H₂S and
15 SO₂ photochemistry in anoxic atmospheres. *Astrophys J* 769:6, doi: 10.1088/0004-
16 637X/769/1/6
- 17 Johnson ML, Burnett DS (1993) SO₂-rock interaction on Io: Reaction under highly oxidizing
18 conditions. *J Geophys Res* 98:1223–1230
- 19 Jugo PJ, Luth RW, Richards JP (2005) Experimental data on the speciation of sulfur as a function
20 of oxygen fugacity in basaltic melts. *Geochim Cosmochim Acta* 69:497–503, doi:
21 10.1016/j.gca.2004.07.011
- 22 King PL et al. (2018) Experimental approaches and theoretical aspects of gas-solid reactions. *Rev*
23 *Mineral Geochem* XX:xxx-xxx
- 24 Knoche R, Dingwell DB, Webb SL (1992) Non-linear temperature dependence of liquid volumes
25 in the system albite-anorthite-diopside. *Contrib Mineral Petrol* 111:61–73, doi:
26 10.1007/BF00296578
- 27 Kumar S (1985) The SO₂ atmosphere and ionosphere of Io: Ion chemistry, atmospheric escape,
28 and models corresponding to the Pioneer 10 radio occultation measurements. *Icarus*
29 61:101–123
- 30 Le Losq C, Neuville DR, Florian P, Henderson GS, Massiot D (2014) The role of Al³⁺ on rheology
31 and structural changes in sodium silicate and aluminosilicate glasses and melts. *Geochim*
32 *Cosmochim Acta* 126:495–517, doi: 10.1016/j.gca.2013.11.010
- 33 Le Losq C, Neuville DR, Massiot D, Greaves GN, Florian P, Chen W, Zhou Z (2017) Percolation
34 channels: a universal idea to describe the atomic structure and dynamics of glasses and
35 melts. *Sci Rep* 7:16490, doi: 10.1038/s41598-017-16741-3
- 36 Lemke KH, Seward TM (2018) Molecular clusters and solvation in volcanic and hydrothermal
37 vapors. *Rev Mineral Geochem* XX:xxx-xxx
- 38 Li EY, Chareev, D. A., Shilobreeva, S. N., Grichuk DV, Tyutyunnik OA (2010) Experimental
39 study of sulfur dioxide interaction with silicates and aluminosilicates at temperatures of
40 650 and 850°C. *Geochim Int* 48:1039–1046

- 1 Li EY, Grichuk DV, Shilobreeva SN, Chareev DA (2011) Interaction between (alumino)silicates
2 and SO₂-containing gas: experiment and thermodynamic model. *Vestn Otd Nauk O Zemle*
3 *RAN* 3:1–7, doi: 10.2205/2011NZ000194
- 4 Luthra KL, Worrell WL (1978) Simultaneous sulfidation-oxidation of nickel at 603°C in argon-
5 SO₂ atmospheres. *Metall Trans A* 9:1055–1061, doi: 10.1007/BF02652209
6 Magnien V, Neuville DR, Cormier L, Roux J, Hazemann J-L, de Ligny D, Pascarelli S, Vickridge I,
7 Pinet O, Richet P (2008) Kinetics and mechanisms of iron redox reactions in silicate melts:
8 The effects of temperature and alkali cations. *Geochim Cosmochim Acta* 72:2157–2168,
9 doi: 10.1016/j.gca.2008.02.007
- 10 Martens RM, Rosenhauer M, Büttner H, von Gehlen K (1987) Heat capacity and kinetic parameters
11 in the glass transformation interval of diopside, anorthite and albite glass. *Chem Geol*
12 62:49–70, doi: 10.1016/0009-2541(87)90057-X
- 13 McCormick BT, Edmonds M, Mather TA, Champion R, Hayer CSL, Thomas HE, Carn SA (2013)
14 Volcano monitoring applications of the Ozone Monitoring Instrument. *Geol Soc Lond*
15 *Spec Publ* 380:259–291, doi: 10.1144/SP380.11
- 16 Misra A, Krissansen-Totton J, Koehler MC, Sholes S (2015) Transient sulfate aerosols as a
17 signature of exoplanet volcanism. *Astrobiology* 15:462–477, doi: 10.1089/ast.2014.1204
- 18 Monceau D, Pieraggi B (1998) Determination of parabolic rate constants from a local analysis of
19 mass-gain curves. *Oxid Met* 50:477–493, doi: 10.1023/A:1018860909826
- 20 Mysen BO, Richet P (2005) *Silicate glasses and melts: properties and structure*. Elsevier,
21 Amsterdam; Boston, 560pp
- 22 Mysen BO, Virgo D, Seifert FA (1982) The structure of silicate melts: Implications for chemical
23 and physical properties of natural magma. *Rev Geophys* 20:353–383, doi:
24 10.1029/RG020i003p00353
- 25 Neuville DR, Cormier L, Massiot D (2006) Al coordination and speciation in calcium
26 aluminosilicate glasses: Effects of composition determined by ²⁷Al MQ-MAS NMR and
27 Raman spectroscopy. *Chem Geol* 229:173–185, doi: 10.1016/j.chemgeo.2006.01.019
- 28 Oelkers EH, Schott J (eds) (2009) *Thermodynamics and kinetics of water-rock interaction*. *Rev*
29 *Mineral Geochem* 70
- 30 O'Neill HSC (1988) Systems Fe-O and Cu-O: thermodynamic data for the equilibria Fe-'FeO', Fe-
31 Fe₃O₄, 'FeO'-Fe₃O₄, Fe₃O₄-Fe₂O₃, Cu-Cu₂O, and Cu₂O-CuO from emf measurements.
32 *Amer Miner* 73:470–486
- 33 O'Neill HSC, Pownceby MI (1993) Thermodynamic data from redox reactions at high
34 temperatures. I. An experimental and theoretical assessment of the electrochemical method
35 using stabilized zirconia electrolytes, with revised values for the Fe-'FeO', Co-CoO, Ni-
36 NiO and Cu-Cu₂O oxygen buffers, and new data for the W-WO₂ buffer. *Contrib Mineral*
37 *Petrol* 114:296–314, doi: 10.1007/BF01046533
- 38 Oppenheimer C, Fischer TP, Scaillet B (2014) 4.4 - Volcanic Degassing: Process and Impact. In:
39 Turekian HDHK (eds) *Treatise on Geochemistry (Second Edition)*. Elsevier, Oxford, pp
40 111–179
41 Ostyn K m., Carter C b., Koehne M, Falke H, Schmalzried H (1984) Internal
42 reactions in oxide solid solutions. *J Am Ceram Soc* 67:679–685, doi: 10.1111/j.1151-
2916.1984.tb19682.x

- 1 Palm AB, King PL, Renggli CJ, Richard LH, Eggins SM, Dalby KN, Mernagh TP, Troitzsch U,
2 Herring A, Beeching L, Kinsley L, Guagliardo P (2018) Revealing mineral formation and
3 major and trace element migration in a basaltic glass reacted with SO_{2(g)} at high
4 temperature. *Rev Mineral Geochem* XX:xxx-xxx
- 5 Pieraggi B (1987) Calculations of parabolic reaction rate constants. *Oxid Met* 27:177–185, doi:
6 10.1007/BF00667057
- 7 Renggli CJ, King PL, Henley RW, McMorro L, Middleton J, Guagliardo P. Gas-solid reactions
8 between SO_{2(g)} and simple glasses in the system Diopside-Anorthite-Albite. In Preparation.
- 9 Robie RA, Hemingway BS (1995) Thermodynamic properties of minerals and related substances
10 at 298.15 K and 1 bar (10⁵ pascals) pressure and at higher temperatures. United States
11 Geological Survey, B-2131, 461pp
- 12 Roselieb K, Jambon A (2002) Tracer diffusion of Mg, Ca, Sr, and Ba in Na-aluminosilicate melts.
13 *Geochim Cosmochim Acta* 69:109-123
- 14 Rowe JJ, Morey GW, Silber CC (1967) The ternary system K₂SO₄-MgSO₄-CaSO₄. *J Inorg Nucl*
15 *Chem* 29:925–942, doi: 10.1016/0022-1902(67)80075-7
- 16 Schmalzried H (1983) Internal and external oxidation of nonmetallic compounds and solid
17 solutions (I). *Berichte Bunsenges Für Phys Chem* 87:551–558, doi:
18 10.1002/bbpc.19830870702
- 19 Schmalzried H, Backhaus-Ricoult M (1993) Internal solid state reactions. *Prog Solid State Chem*
20 22:1–57, doi: 10.1016/0079-6786(93)90007-E
- 21 Schreiber HD (1987) An electrochemical series of redox couples in silicate melts: A review and
22 applications to geochemistry. *J Geophys Res Solid Earth* 92:9225–9232, doi:
23 10.1029/JB092iB09p09225
- 24 Schwab RG, Küstner D (1981) Die Gleichgewichtsfugazitäten technologisch und petrologisch
25 wichtiger Sauerstoffpuffer. *Neues Jahrb Für Mineral - Abh* 140:111–142
- 26 Shannon RD (1976) Revised effective ionic radii and systematic studies of interatomic distances
27 in halides and chalcogenides. *Acta Crystallogr A* 32:751–767
- 28 Shinohara H (2013) Volatile flux from subduction zone volcanoes: Insights from a detailed
29 evaluation of the fluxes from volcanoes in Japan. *J Volcanol Geotherm Res* 268:46–63,
30 doi: 10.1016/j.jvolgeores.2013.10.007
- 31 Sobiech M, Wohlschlägel M, Welzel U, Mittemeijer EJ, Hügel W, Seekamp A, Liu W, Ice GE
32 (2009) Local, submicron, strain gradients as the cause of Sn whisker growth. *Appl Phys*
33 *Lett* 94:221901, doi: 10.1063/1.3147864
- 34 Sossi P, Fegley B (2018) Gas-condensed phase interactions in planetary science: Thermodynamics
35 and applications. *Rev Mineral Geochem* XX:xxx-xxx
- 36 Stern KH, Weise EL (1966) High temperature properties and decomposition of inorganic salts. Part
37 1. Sulfates. National Bureau of Standards Tolpygo VK, Clarke DR (1998a) Wrinkling of
38 α -alumina films grown by thermal oxidation—I. Quantitative studies on single crystals of
39 Fe–Cr–Al alloy. *Acta Mater* 46:5153–5166, doi: 10.1016/S1359-6454(98)00133-5

1 Tolpygo VK, Clarke DR (1998b) Wrinkling of α -alumina films grown by oxidation—II. Oxide
2 separation and failure. *Acta Mater* 46:5167–5174, doi: 10.1016/S1359-6454(98)00134-7

3 Tröger WE (2017) *Optische Bestimmung der gesteinsbildenden Minerale Teil I: Bestimmungstabellen*. 5th edition, Schweizerbart Science Publishers, Stuttgart, Germany,
4 188pp
5

6 Wang A, Freeman JJ, Jolliff BL, Chou I-M (2006) Sulfates on Mars: A systematic Raman
7 spectroscopic study of hydration states of magnesium sulfates. *Geochim Cosmochim Acta*
8 70:6118–6135, doi: 10.1016/j.gca.2006.05.022

9 Webb S (1997) Silicate melts: Relaxation, rheology, and the glass transition. *Rev Geophys* 35:191–
10 218, doi: 10.1029/96RG03263

11 Wendlandt RF (1991) Oxygen diffusion in basalt and andesite melts: experimental results and
12 discussion of chemical versus tracer diffusion. *Contrib Mineral Petrol* 108:463–471, doi:
13 10.1007/BF00303450

14 Wilke M (2005) Fe in magma—An overview. *Ann Geophys* 48:609–617

15 Wilke M, Farges F, Partzsch GM, Schmidt C, Behrens H (2007) Speciation of Fe in silicate glasses
16 and melts by in-situ XANES spectroscopy. *Am Mineral* 92:44–56

17 Wilke M, Klimm K, Kohn SC (2011) Spectroscopic studies on sulfur speciation in synthetic and
18 natural glasses. *Rev Mineral Geochem* 37:41–78

19 Zhang Y (2010) Diffusion in minerals and melts: Theoretical background. *Rev Mineral Geochem*
20 72:5–59, doi: 10.2138/rmg.2010.72.2

21 Zolotov M (2018) Gas-solid interactions on Venus and other solar system bodies. *Rev Mineral*
22 *Geochem* XX:xxx-xxx

23

24

FIGURE CAPTIONS

25 **Figure 1.** Equilibrium speciation of $\text{SO}_{2(g)}$ at 1 bar and temperatures from 500 to 1300 °C. The
26 speciation was calculated using a Gibbs free energy minimization approach based on the JANAF
27 database (Chase 1998) using the program HSC8 from Outotec. $\text{SO}_{2(g)}$ dissociates to $\text{SO}_{3(g)}$, $\text{SO}_{(g)}$,
28 $\text{O}_{2(g)}$ and sulfur allotropes, the most prominent of which are $\text{S}_{2(g)}$ and $\text{S}_{3(g)}$. The mole fraction of
29 $\text{O}_{2(g)}$ is equivalent to its oxygen fugacity ($f\text{O}_2$) under the condition of ideal gas behavior.

30 **Figure 2.** Scanning electron microscopy images of surface coatings (view from top) formed in
31 reactions between $\text{SO}_{2(g)}$ and glasses. a) Well crystallized platy CaSO_4 crystals formed on a tephrite
32 glass reacted for 1 hour at 800 °C with gas mixture of 1% $\text{SO}_{2(g)}$, air and He gas (Figure provided
33 by Paul Ayris, Ayris et al. 2013). b) Discontinuously distributed Na_2SO_4 grains on a soda-lime
34 glass reacted with $\text{SO}_{2(g)}$ for 21 days at 600 °C. The large crystals cover a scratch in the unreacted
35 glass surface, which resulted in a higher surface area and an associated higher degree of reaction
36 (Used by permission of the American Geophysical Union, from Burnett et al. 1997, *Journal of*
37 *Geophysical Research*, Vol. 102, Fig. 5, p. 19378).

38 **Figure 3.** Discontinuous sulfate coating on glass surfaces reacted with $\text{SO}_{2(g)}$. a) SEM image (view
39 from top) of the discontinuous Na_2SO_4 coating on an albite glass surface reacted with $\text{SO}_{2(g)}$ at 600
40 °C for 1 hour. The sulfate grains show facets. Individual crystals are commonly connected to one

1 or more surrounding grains forming small clusters. b) A schematic cross-section showing how in
2 the case of discontinuous coatings parts of the silicate glass surface remain exposed to the gas phase
3 allowing the reaction to proceed. In this type of reaction the diffusion of cations in the glass to the
4 surface is the rate controlling mechanism (Renggli et al. in prep.).

5 **Figure 4.** Continuous sulfate coatings observed on the surfaces of some Fe-free glasses. a) SEM
6 image of the anhydrite coating on an anorthite glass surface reacted with $\text{SO}_{2(g)}$ at 800 °C for 1
7 hour. b) Backscattered electron image of the coating on an Fe-free basalt glass reacted with $\text{SO}_{2(g)}$
8 at 700 °C for 24 hours. The brighter euhedral grains are anhydrite, whereas the darker material is
9 MgSO_4 which was partially hydrated in air after the experiment. c) Schematic drawing of the
10 reaction forming continuous coatings. After initial coating the glass is no longer directly exposed
11 to the gas, such that an additional mechanism is required to transport the gas and/or the cations
12 through the coating for ongoing sulfate formation. When growth occurs within the coating the
13 grains accumulate stress which can result in the deformation of the coating (see Fig. 5). The
14 outward diffusion of cations results in a depletion in the glass which can cause destabilization, and
15 in some nucleation and crystallization near the surface.

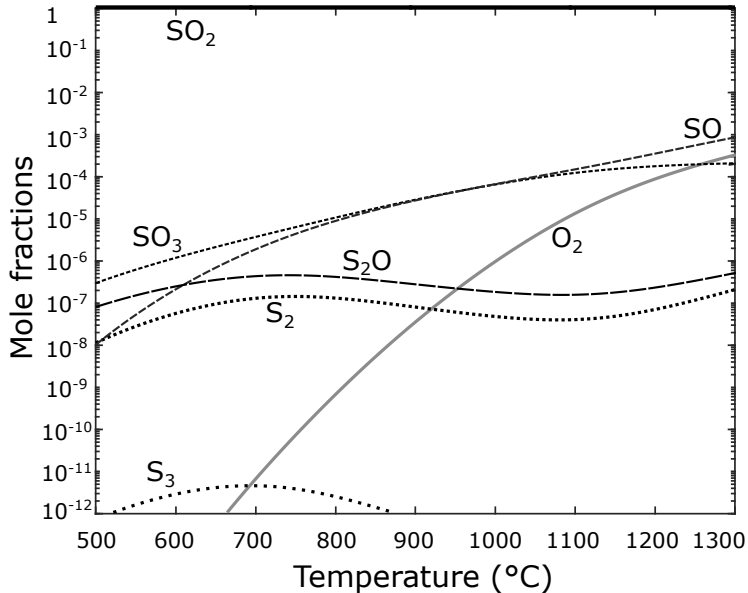
16 **Figure 5.** Images a, b and c show SEM images of deformed continuous anhydrite coatings on Fe-
17 free glasses. The coatings shown in a and c were formed on the eutectic $\text{An}_{36}\text{-Di}_{64}$ glass reacted at
18 800 °C for 24 hours. Image b shows the coating of anhydrite on an $\text{Ab}_{73}\text{An}_{27}$ glass reacted at 700 °C
19 for 24 hours. The drawings d, e and f schematically represent how the respective textures imaged
20 in a, b and c developed. All of the textures are the result of stress accumulation within the coating
21 due to internal sulfate growth as shown in Figure 4. In the first case, whiskers can be formed by
22 epitactic overgrowth at grain boundaries and triple junctions (a and d). In the second case, laterally
23 expanding crystals in the coating have bent upwards at grain boundaries resulting in the imaged
24 “chicken-wire” texture (b and e). A third texture type forms as thick polycrystalline sulfate layers
25 continue to grow they detach from the glass surface and wrinkle and buckle (c and f).

26 **Figure 6.** Back-scattered electron images of coatings formed on Fe-bearing basaltic glasses which
27 were pre-equilibrated at different $f\text{O}_2$. The textures and assemblages vary considerably as a
28 function of the pre-equilibration. The observed phases are labelled as: gl.: substrate glass; Ca:
29 CaSO_4 ; Mg: MgSO_4 ; Na: Na_2SO_4 ; hem: Fe_2O_3 ; FeTi-ox: Fe-Ti-oxide. All three textures are not
30 continuous and in some areas parts of the glass substrate can be observed (gl.). a) Tholeiitic basalt
31 (NNO-1.5, 700 °C, 24h) is coated with CaSO_4 (forming brighter crystals, Ca), hydrated MgSO_4 (in
32 darker greys, Mg), and sub-micron sized Fe-oxides (hem and FeTi-ox). b) Tholeiitic basalt (NNO,
33 700 °C, 24h), coated with large columnar CaSO_4 (Ca), hydrated MgSO_4 (darker grey in the lower
34 left corner of the image, Mg), Na_2SO_4 (Na) in between CaSO_4 and mixed into the MgSO_4 , and
35 Fe_2O_3 (bright white, hem). Some Fe-oxides contain significant amounts of Ti (FeTi-ox). c)
36 Tholeiitic basalt (NNO+1, 700 °C, 24h) coated with large columnar CaSO_4 (Ca), fine-grained
37 Na_2SO_4 (Na) mixed with sub-microns sized Fe-oxides, and larger Fe-oxides (hem) including some
38 Fe-Ti-oxides (FeTi-ox). No MgSO_4 occurs in this coating.

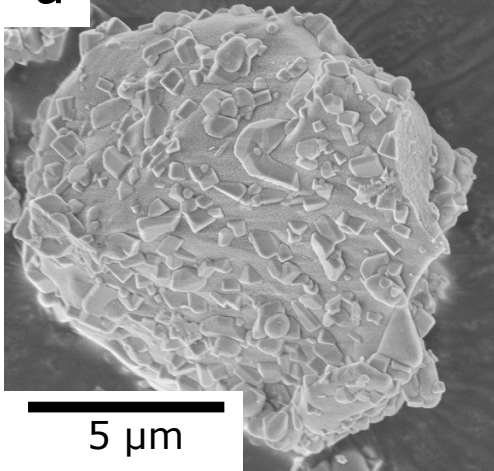
39 **Figure 7.** NanoSIMS maps of major elements in a cross-section of a tholeiitic basalt (NNO, 700 °C,
40 24h). The dashed line shows the location of the interface between the basaltic glass to the right and
41 the sulfate coating to the left. a) Si: The network-forming cation remains in the glass and is possibly
42 slightly enriched just beneath the surface, whereas it is not detected in the coating. b) Ti: Ti is not
43 detected in the coating material in this cross-section, even though Ti-bearing Fe-oxides were
44 observed in the coating. c) Mg: Mg is predominantly retained in the glass substrate. Mg-rich zones
45 occur as rings surrounding more depleted Fe-rich nuclei. d) Fe: Fe forms spherulites which are
46 relatively depleted in Ti, Mg and Ca, but slightly enriched in Na. The number of spherulites
47 increases toward the original surface of the glass (dashed line). This cross-section has not sampled
48 a Fe-oxide grain in the coating. e) Na: Na is a major component of the coatings and is also enriched
49 in the substrate towards the surface. f) Ca: Ca is depleted in the glass substrate with decreasing
50 concentrations towards the surface and enriched in the coating.

1 **Figure 8.** Phase relationships in the system Fe-S-O as a function of $f\text{SO}_2$ and $f\text{O}_2$ calculated from
2 the equilibrium constants of equations 5 to 13 at 700 °C and 1 bar. Fe-phases observed in coatings
3 of $\text{SO}_{2(g)}$ experiments are Fe_2O_3 in most cases and assemblages including both Fe_2O_3 and Fe_3O_4
4 (Palm et al. 2018) as indicated by the box at $\log f\text{SO}_2$ near 0. The figure also shows the $\log f\text{O}_2$ of
5 the NNO redox buffer relative to which some of the reacted basalt glasses were pre-equilibrated.
6 The geometric relationship of the phase boundaries remains constant with temperature. At 700 °C
7 and 1 bar the fugacities of minor gas species in equilibrium with $\text{SO}_{2(g)}$ (see Fig. 1) are $\log f\text{O}_2=-$
8 12.1, $\log f\text{S}_2=-7$, $\log f\text{S}_3=-11.4$, $\log f\text{SO}_3=-5.7$, $\log f\text{SO}=-6.1$ and $\log f\text{S}_2\text{O}=-6.5$. The calculations were
9 made using the package HSC8 by Outotec based on the JANAF database (Chase 1998).

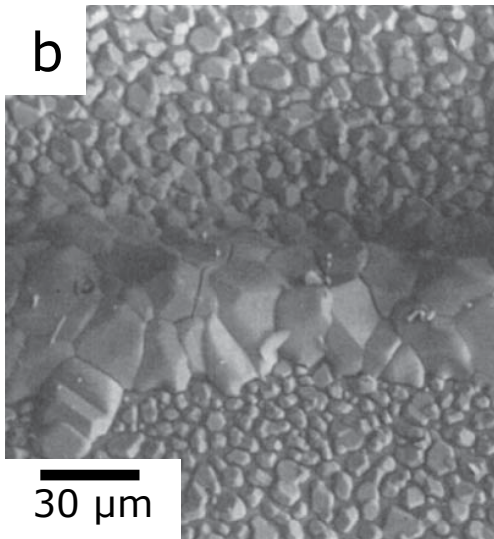
10 **Figure 9.** Schematic drawings of the reaction between gases and Fe-bearing silicate glasses at 700
11 °C and 1 bar. a) $\text{SO}_{2(g)}$ reaction results in the formation of sulfate and oxide coatings. The oxidation
12 of Fe in the glass occurs via the inward diffusion of electron holes and the outward diffusion of
13 alkali and alkaline earth cations, forming the sulfates. The glass subsurface is relatively enriched
14 in Si and Al (network-forming cations) due to the diffusive loss of other cations. The change in the
15 chemical composition of the glass results in the crystal nucleation near the glass surface. b) $\text{O}_{2(g)}$
16 reaction with Fe-bearing silicate glasses requires the outward diffusion of alkaline earths and
17 inward diffusion of electron holes. Na diffuses into the oxidizing surface layer to stabilize
18 tetrahedrally coordinated ferric iron. Insufficient charge balancing of ferric iron can result in the
19 destabilization of the glass and the nucleation of oxides and silicates (Cook et al. 1990; Cooper et
20 al. 1996b, a; Cook and Cooper 2000; Burkhard 2001).



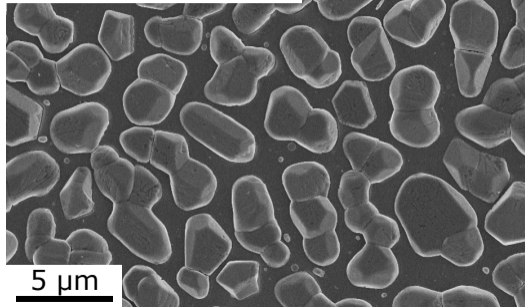
a



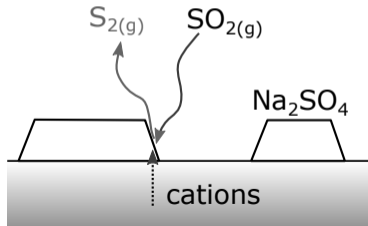
b



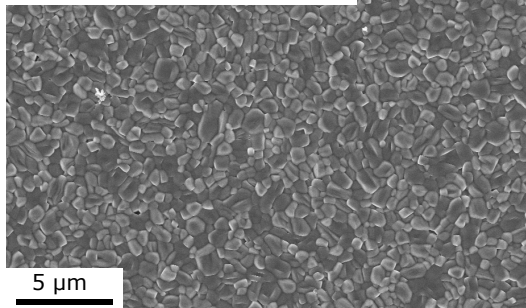
a) Albite, 600 °C, 1h



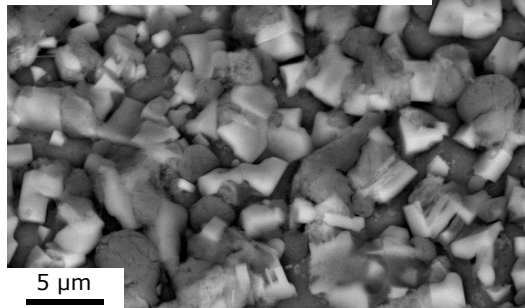
b) growth of single crystals



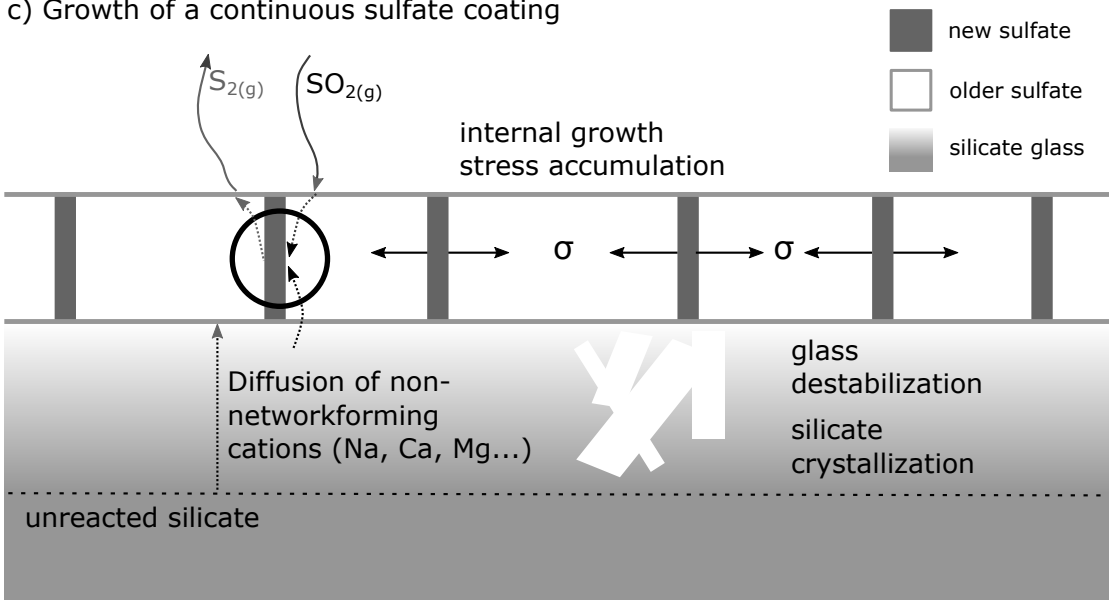
a) Anorthite, 800 °C, 1h

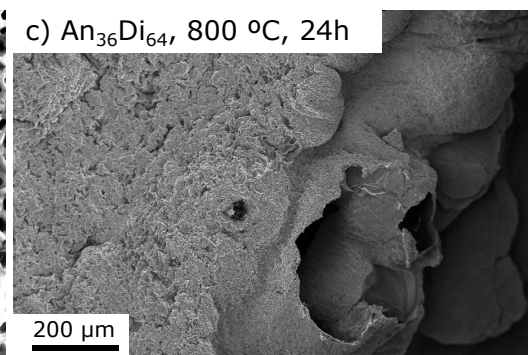
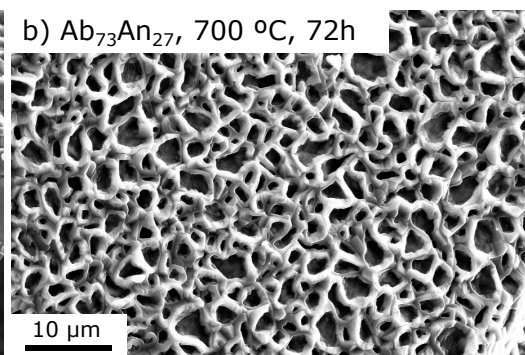
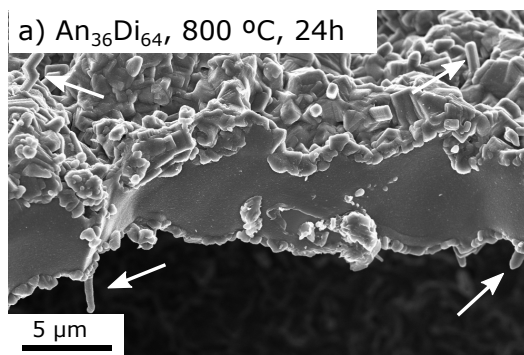


b) Fe-free basalt, 700 °C, 24h

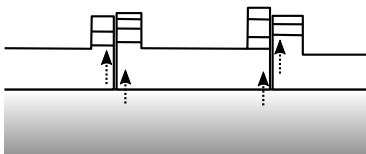


c) Growth of a continuous sulfate coating

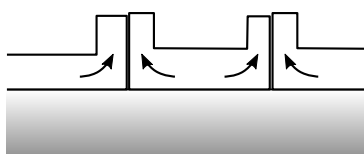




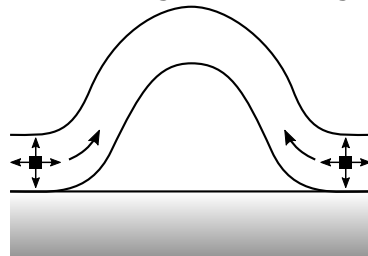
d) epitactic overgrowth at grain boundaries



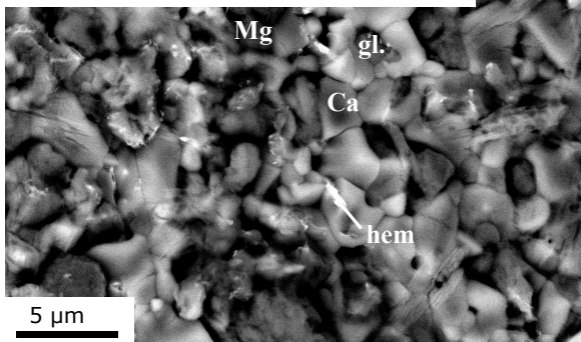
e) lateral growth of single crystals



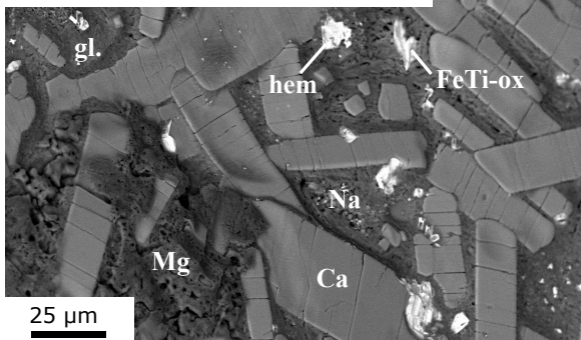
f) polycrystalline layer, wrinkling and buckling



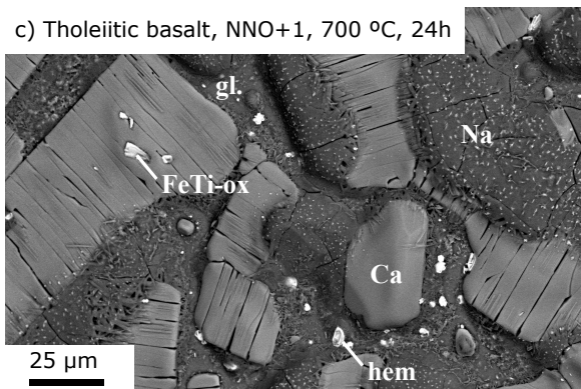
a) Tholeiitic basalt, NNO-1.5 700 °C, 24h

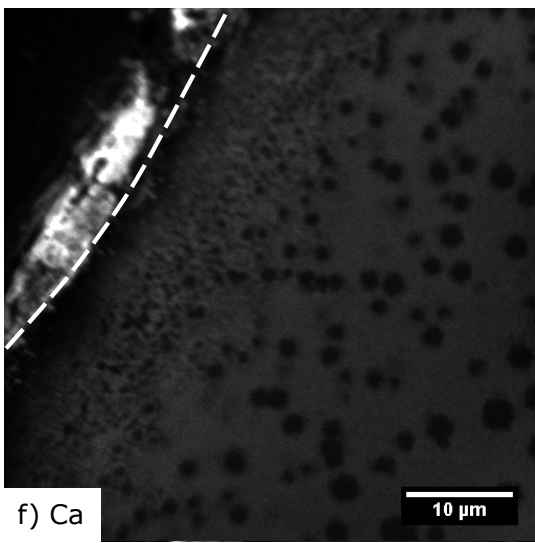
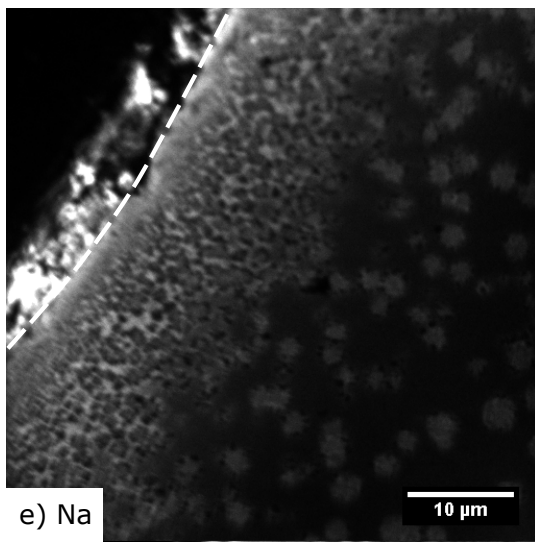
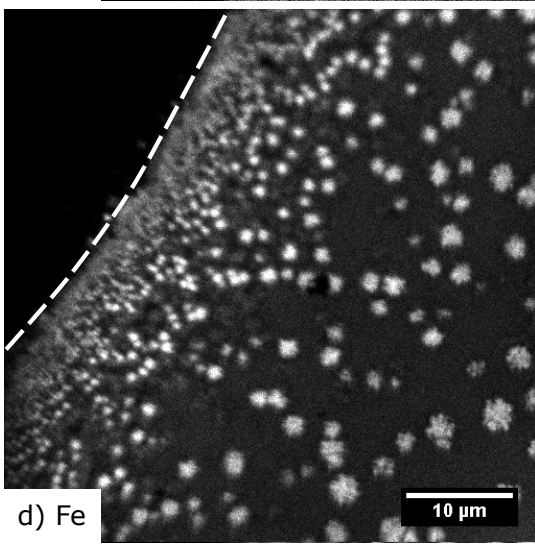
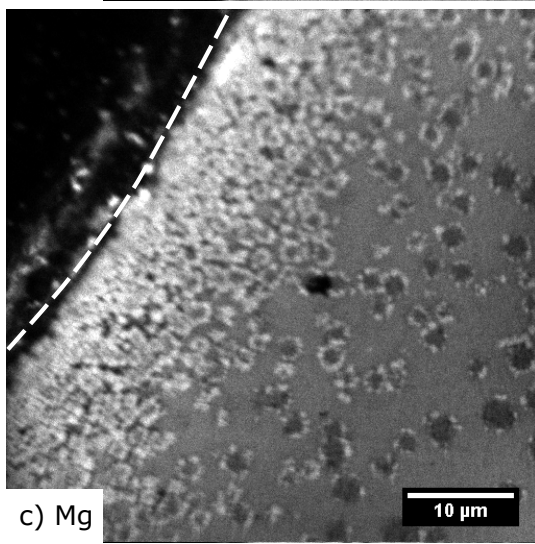
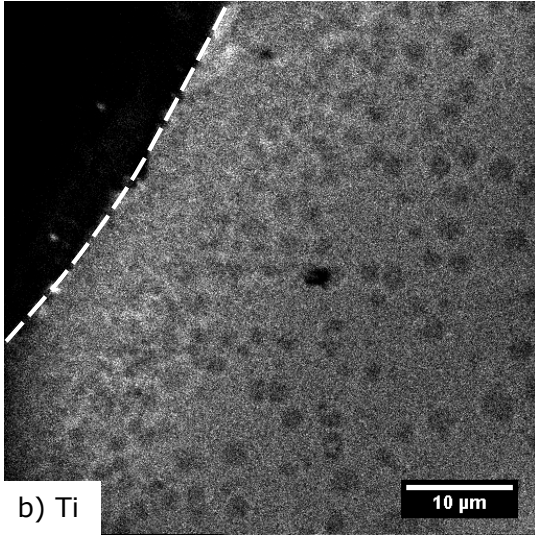
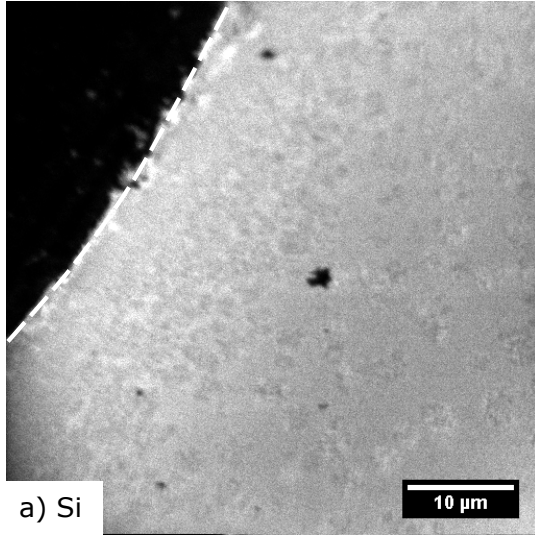


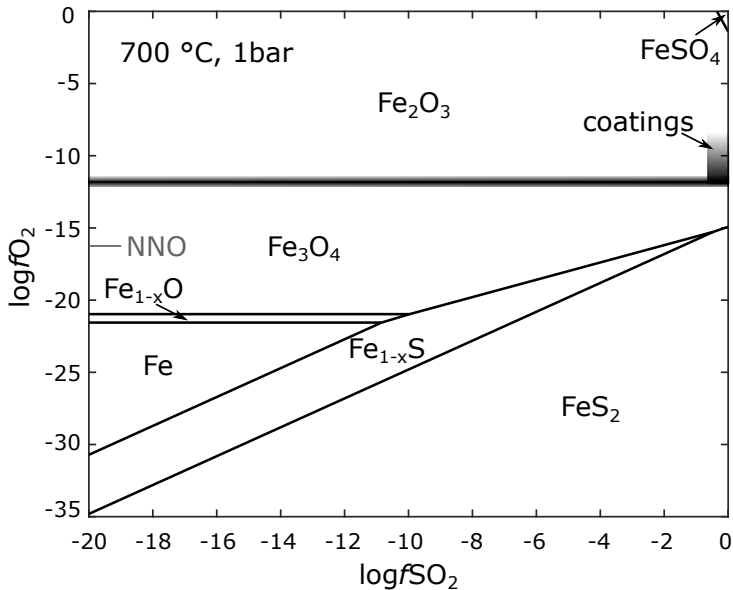
b) Tholeiitic basalt, NNO, 700 °C, 24h



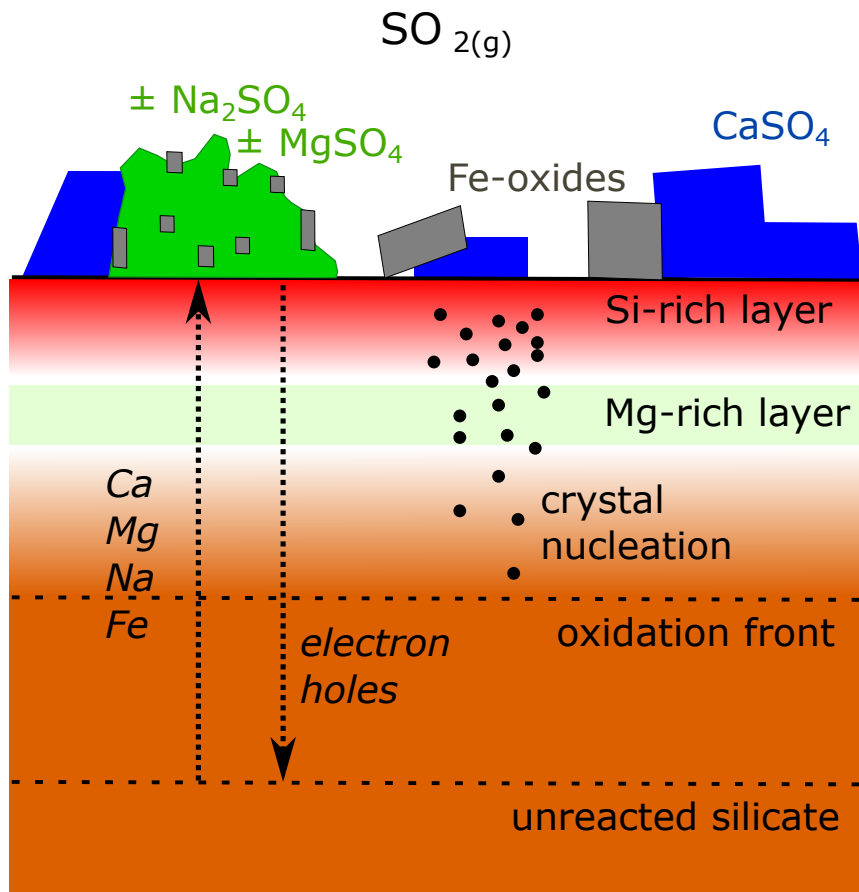
c) Tholeiitic basalt, NNO+1, 700 °C, 24h







a) SO₂-reaction, Fe-bearing glass



b) O₂-reaction, Fe-bearing glass

